

A Search for Supersymmetry in Events with
Photon and Jets from Proton-Proton Collisions
at $\sqrt{s} = 7\text{TeV}$ with the CMS Detector

Robin J. Nandi

March 5, 2012

Contents

| | |
|--|-----------|
| 1 Theory | 4 |
| 1.1 Introduction | 4 |
| 1.2 The Standard Model | 4 |
| 1.3 Gauge Symmetries of the Standard Model | 6 |
| 1.3.1 Quantum Electrodynamics (QED) | 7 |
| 1.3.2 The Electroweak Sector | 8 |
| 1.3.3 Quantum Chromodynamics (QCD) | 12 |
| 1.4 Motivation for new physics at the TeV scale | 15 |
| 1.4.1 WW scattering | 15 |
| 1.4.2 New energy scale | 16 |
| 1.4.3 Hierarchy Problem | 16 |
| 1.4.4 Dark Matter candidates | 17 |
| 1.5 Supersymmetry | 18 |
| 1.6 Strong production Gauge Mediated SUSY breaking | 18 |
| 2 CMS Detector and Reconstruction | 20 |
| 2.1 Introduction | 20 |
| 2.2 Pixel Detector | 21 |
| 2.3 Silicon Strip Tracker | 24 |
| 2.4 Electromagnetic Calorimeter | 25 |
| 2.5 Hadronic Calorimeter | 29 |
| 2.6 Superconducting Solenoid Magnet | 31 |
| 2.7 Muon System | 32 |
| 2.8 Trigger | 33 |
| 2.9 CMS Computing Model | 34 |

| | | |
|----------|--|-----------|
| 2.10 | Photon Reconstruction | 34 |
| 2.11 | Jet Reconstruction | 37 |
| 3 | Data, Trigger and Event Selection | 38 |
| 3.1 | Data | 38 |
| 3.2 | Monte Carlo Samples | 40 |
| 3.3 | Trigger | 42 |
| 3.4 | Photon Selection | 44 |
| 3.5 | Jet Selection | 44 |
| 3.6 | Missing Transverse Energy | 47 |
| 3.7 | Event Selection | 48 |
| 4 | Background Estimation | 52 |
| 4.1 | Introduction | 52 |
| 4.2 | QCD Background | 53 |
| 4.3 | Electroweak and $t\bar{t}$ Backgrounds | 58 |
| 4.4 | Conclusions | 58 |
| 5 | Signal Prediction and Systematics | 59 |
| 5.1 | Introduction | 59 |
| 5.2 | Photon Efficiency Correction | 60 |
| 5.3 | Jet Energy Scale | 62 |
| 5.4 | Jet Energy Resolution | 66 |
| 5.5 | Pile-up | 70 |
| 5.6 | Signal Cross-Section | 77 |
| 5.7 | Integrated Luminosity | 77 |
| 5.8 | Summary of Systematics | 79 |
| 6 | Limit Setting and Results | 80 |
| 6.1 | Introduction | 80 |
| 6.2 | Likelihood Function | 81 |
| 6.3 | Systematic Uncertainties | 82 |
| 6.4 | Test Statistic | 82 |
| 6.5 | Confidence Intervals | 83 |
| 6.5.1 | Wilks Theorem | 83 |

| | | |
|----------|--|-----------|
| 6.5.2 | Neyman Construction | 83 |
| 6.5.3 | CLs: MC toys with hypothesis testing | 84 |
| 6.6 | Expected and Observed Limit | 84 |
| 7 | Conclusions and Further Work | 86 |
| | References | 87 |

Chapter 1

Theory

1.1 Introduction

In this chapter a brief historical background of the Standard Model is given with some of the results that inform our current understanding. The role of symmetry in particle physics is discussed and the gauge structure of the Standard Model is examined. The motivation for new physics at the TeV scale is considered. A brief description of supersymmetry, a popular possible extension to the Standard Model, is given and the ideas behind it are discussed. Finally, the current exclusion limits on Gauge Mediated SUSY Breaking are reviewed.

1.2 The Standard Model

The Standard Model of particle physics contains our theoretical knowledge of the fundamental particles and the forces between them. Figure 1.1 shows the fundamental particles and the force carriers according to our current knowledge.

Historically the Standard Model was formed by trying to understand atomic spectra. In 1928 Dirac came up with the Dirac equation to describe fermions, which was the first theory to deal with relativity and quantum mechanics. Later QED a theory of the interactions of light with matter was developed by Richard Feynman (among others) which explained the Lamb shift in Hydrogen and made a very precise prediction for the magnetic moment of the electron.

| Three Generations of Matter (Fermions) | | | |
|--|----------------------|----------------------|--------------------|
| | I | II | III |
| mass \rightarrow | 2.4 MeV | 1.27 GeV | 171.2 GeV |
| charge $\rightarrow \frac{2}{3}$ | u | c | t |
| spin $\rightarrow \frac{1}{2}$ | up | charm | top |
| name \rightarrow | | | |
| Quarks | d | s | b |
| | down | strange | bottom |
| 4.8 MeV | 104 MeV | 4.2 GeV | 0 |
| $-\frac{1}{3}$ | $\frac{1}{3}$ | $-\frac{1}{3}$ | 0 |
| Leptons | v _e | v _μ | v _τ |
| | electron neutrino | muon neutrino | tau neutrino |
| $< 2.2 \text{ eV}$ | $< 0.17 \text{ MeV}$ | $< 15.5 \text{ MeV}$ | 91.2 GeV |
| 0 | 0 | 0 | 0 |
| $\frac{1}{2}$ | $\frac{1}{2}$ | $\frac{1}{2}$ | 1 |
| e | μ | τ | Z |
| electron | muon | tau | weak force |
| 0.511 MeV | 105.7 MeV | 1.777 GeV | 80.4 GeV |
| -1 | -1 | -1 | ± 1 |
| $\frac{1}{2}$ | $\frac{1}{2}$ | $\frac{1}{2}$ | 1 |
| Bosons (Forces) | | | |
| | | | |
| | | | |

Figure 1.1: The fundamental particles according to the Standard Model.

The neutrino was postulated by Pauli in 1930 to explain the continuous electron energy spectrum in β -decay. Neutrinos were discovered by direct detection in 1956 by beta capture in a huge detector of water with CdCl_2 dissolved in it by the Savannah River nuclear reactor. Three flavours of neutrinos corresponding to each of the leptons has been discovered. More recently neutrino oscillations have been observed in which neutrinos can change flavour. The flavour change happens due to a difference between the mass eigenstates and the flavour eigenstates indicating that neutrinos have a non-zero mass.

After the discovery of many new hadrons, e.g. π , K , Δ , Σ , it became clear that the neutron and proton are not fundamental particles, but made up of more basic constituents. Gell-Mann came up with the quark model in which all hadrons are made up of quarks. There are 6 flavours of quarks with different masses: u, d, c, s, t, b. Each flavour of quark comes in three different colors. Quarks carry color charge and form an $SU(3)$ color triplet. Quarks are not observed as free particles, but only in colorless bound states.

A beautiful experiment by C. S. Wu and collaborators showed that parity is violated in weak interactions. The beta decay of Co⁶⁰ was performed in a magnetic field and at low temperature to polarise the nuclei and the angular distribution of electrons was measured. An asymmetry in the distribution between θ and $180^\circ - \theta$ (where θ is the angle between the electron momentum and the orientation of the parent nucleus) was observed providing unequivocal proof that parity is not conserved in beta decay. This is represented in the Standard Model by the presence of chiral fermions in the structure of the weak interaction.

Electroweak theory was introduced by Glashow, Salam and Weinberg who proposed that the electromagnetic force and the weak force are parts of the same theory. The W^\pm and Z^0 bosons were predicted to have masses in the ratio $\frac{m_W}{m_Z} = \cos \theta_W$, where θ_W is the weak mixing angle. The W^\pm and Z^0 bosons were discovered by the UA1 and UA2 experiments at CERN. Carlo Rubbia and Simon van der Meer won the Nobel Prize for Physics in 1983 for their decisive contributions toward the discovery.

The Large Electron Positron Collider (LEP) made e^+e^- collisions to search for new physics and make precision electroweak measurements. The collision centre of mass energy could be tuned to generate a resonance of Z bosons. Looking at the Z width for decays to invisible particles relative to the total Z width indicates that there are exactly three flavours of neutrino into which the Z can decay.

1.3 Gauge Symmetries of the Standard Model

There is an important connection between symmetries and conservation laws discovered by Noether [17].

For every symmetry of the theory there is a conserved quantity.

Invariance under translations in time and space give rise to energy and momentum conservation. Invariance under rotation gives rise to conservation of angular momentum. Together with Lorentz invariance these transformations form the

Poincare group. Describing symmetries in terms of group theory was developed by Galois in the 19th Century and was initially used to test the solvability of polynomial equations [2]. These symmetries are all global symmetries meaning that the transformation is the same for all space-time points.

A theory can be described by a Lagrangian which is equal to the kinetic energy minus the potential energy. The equations of motion of such a theory can be derived by minimising the action (Equation 1.1).

$$S = \int L d^4x^\mu \quad (1.1)$$

Consider a Lagrangian with N scalar fields $\phi(x^\mu) = (\phi_1(x^\mu), \dots, \phi_N(x^\mu))$, where x^μ is the space-time co-ordinate as in Equation 1.2.

$$L = L(\phi, \partial_\mu \phi, x^\mu) \quad (1.2)$$

Suppose that this Lagrangian is invariant under the gauge transformation given in Equation 1.3, where the phase is composed of the parameters $\epsilon^a(x^\mu)$ and the generators of the Lie group T^a . This is a gauge symmetry rather than a global symmetry since the phase depends on the space-time point.

$$\phi(x^\mu) \rightarrow \phi(x^\mu) e^{-i\epsilon^a T^a} \quad (1.3)$$

Noether's theorem gives a powerful way of constructing theories based on symmetry which underpins the structure of the standard model. The gauge symmetry of the Standard Model is $SU(3) \times SU(2) \times U(1)$. $SU(3)$ corresponds to QCD and $SU(2) \times U(1)$ corresponds to the electroweak sector. Much of the structure of the Standard Model can be understood by considering the gauge groups.

1.3.1 Quantum Electrodynamics (QED)

The QED Lagrangian for electromagnetic interactions of electrons can be written as Equation 1.4.

$$L = -\frac{1}{4} F_{\mu\nu} F^{\mu\nu} + \bar{\psi} \gamma^\mu D_\mu \psi - m_e \bar{\psi} \psi \quad (1.4)$$

| Group | Fields | Strength | Generators |
|-------|-----------|----------|----------------------------|
| SU(2) | A_μ^a | g | $T^a = \frac{\sigma^a}{2}$ |
| U(1) | B_μ | g' | $Y = \frac{1}{2}$ |

Table 1.1: Definitions of the symbols representing the properties of the electroweak groups. $a = 1, 2, 3$ and σ^a are the Pauli matrices.

The first term represents the free electromagnetic field. $F_{\mu\nu} = \partial_\mu A_\nu - \partial_\nu A_\mu$, where A_μ is the electromagnetic vector potential. The second term represents the electron kinetic energy and the interaction between electron and photon. $D_\mu = \partial_\mu - ieA_\mu$ is the covariant derivative (i.e. it remains the same under the gauge transformation). The third term represents the mass of the electron. This lagrangian is invariant under the U(1) gauge transformation given by Equation 1.6.

$$\psi \rightarrow e^{-i\alpha(x)}\psi \quad (1.5)$$

$$A_\mu \rightarrow A_\mu + \frac{1}{e}\partial_\mu\alpha(x) \quad (1.6)$$

The mass term for the electron is allowed by gauge invariance, but a mass term for the photon is forbidden. Also photon self-interactions are forbidden by gauge invariance. The constraints set by gauge invariance tell us a lot about the nature of the electromagnetic interaction. The photon is a massless particle which interacts with electrons, but not with itself. The electromagnetic force has infinite range.

1.3.2 The Electroweak Sector

The electroweak force consists of SU(2) weak isospin and U(1) hypercharge. Table 1.1 defines the symbols for the groups, the corresponding fields and the generators.

Consider a scalar field doublet, ϕ , with respect to SU(2) with U(1) hypercharge $Y = \frac{1}{2}$. The bosonic sector of the electroweak lagrangian can be written as:

$$L = -\frac{1}{4}F_{\mu\nu}^a F_{\mu\nu}^a - \frac{1}{4}G_{\mu\nu} G_{\mu\nu} + (D_\mu \phi)^\dagger (D_\mu \phi) - \lambda \left(\phi^\dagger \phi - \frac{v^2}{2} \right) \quad (1.7)$$

where

$$F_{\mu\nu}^a = \partial_\mu A_\nu^a - \partial_\nu A_\mu^a + g\epsilon^{abc} A_\mu^b A_\nu^c \quad (1.8)$$

$$G_{\mu\nu} = \partial_\mu B_\nu - \partial_\nu B_\mu \quad (1.9)$$

$$D_\mu \phi = \partial_\mu \phi - i\frac{g}{2}\sigma^a A_\mu^a \phi - i\frac{g'}{2}B_\mu \phi \quad (1.10)$$

There is a continuum of ground states giving equivalent physics, one of which must be chosen by nature. This is known as symmetry breaking. Arbitrarily choose:

$$A_\mu = 0 \quad B_\mu = 0 \quad \phi_0 = \frac{v}{\sqrt{2}} \begin{pmatrix} 0 \\ 1 \end{pmatrix} \quad (1.11)$$

Finding the unbroken generator, Q , such that $Q\phi_0 = 0$ and Q is hermitian gives:

$$Q = \begin{pmatrix} 1 & 0 \\ 0 & 0 \end{pmatrix} \quad (1.12)$$

or

$$Q = T^3 + Y \quad (1.13)$$

The unbroken generator corresponds to the subgroup $U(1)_{em}$ of $SU(2) \times U(1)$. This should correspond to a massless gauge field – the electromagnetic field. $U(1)_{em}$ is not the same as the $U(1)$ component in $SU(2) \times U(1)$ so the electromagnetic potential, A_μ (without superscript) is not B_μ , but a linear combination of the fields A_μ^3 and B_μ .

Consider small perturbations around the ground state:

$$\phi = \begin{pmatrix} 0 \\ \frac{v}{\sqrt{2}} + \frac{\chi(x)}{\sqrt{2}} \end{pmatrix} \quad (1.14)$$

Thus we get the following expression for $D_\mu \phi$:

$$D_\mu \phi = \begin{pmatrix} -\frac{ig}{2\sqrt{2}} (A_\mu^1 - iA_\mu^2) (v + \chi(x)) \\ -\frac{i}{2\sqrt{2}} (g' B_\mu - g A_\mu^3) (v + \chi(x)) + \frac{1}{\sqrt{2}} \partial_\mu \chi(x) \end{pmatrix} \quad (1.15)$$

Introduce new fields:

$$W_\mu^\pm = \frac{1}{\sqrt{2}}(A_\mu^1 \mp A_\mu^2) \quad (1.16)$$

$$Z_\mu = \frac{1}{\sqrt{g^2 + g'^2}}(gA_\mu^3 - g'B_\mu) = \cos\theta_W A_\mu^3 - \sin\theta_W B_\mu \quad (1.17)$$

$$A_\mu = \frac{1}{\sqrt{g^2 + g'^2}}(gB_\mu - g'A_\mu^3) = \sin\theta_W A_\mu^3 + \cos\theta_W B_\mu \quad (1.18)$$

Z_μ and A_μ are rotations of the original fields with angle θ_W which satisfies Equation 1.19.

$$\cos\theta_W = \frac{g}{\sqrt{g^2 + g'^2}} \quad \sin\theta_W = \frac{g'}{\sqrt{g^2 + g'^2}} \quad (1.19)$$

Z_μ and A_μ are determined by the necessity that the covariant derivative, $D_\mu\phi$, does not contain A_μ – it must be invariant under the electromagnetic gauge transformation. To quadratic order the lagrangian can be written as:

$$L = -\frac{1}{2}\mathcal{W}_{\mu\nu}^+\mathcal{W}_{\mu\nu}^- + m_W^2 W_\mu^+ W_\mu^- \quad (1.20)$$

$$-\frac{1}{4}\mathcal{Z}_{\mu\nu}\mathcal{Z}_{\mu\nu} + \frac{m_Z^2}{2}Z_\mu Z_\mu \quad (1.21)$$

$$-\frac{1}{4}F_{\mu\nu}F_{\mu\nu} \quad (1.22)$$

$$+\frac{1}{2}(\partial_\mu\chi)^2 - \frac{m_\chi^2}{2}\chi^2 \quad (1.23)$$

where

$$\mathcal{W}_{\mu\nu}^\pm = \partial_\mu W_\nu^\pm - \partial_\nu W_\mu^\pm \quad (1.24)$$

$$\mathcal{Z}_{\mu\nu} = \partial_\mu Z_\nu - \partial_\nu Z_\mu \quad (1.25)$$

The physical fields can be seen from the lagrangian and are summarised in Table 1.2.

The electroweak theory of Glashow, Salam and Weinberg predicted mixing between the electromagnetic and weak forces and the existence of W^\pm and Z^0 bosons with masses in the ratio given by Equation 1.26.

$$\frac{m_W}{m_Z} = \cos\theta_W \quad (1.26)$$

| Field | Mass | Particle |
|-------------|--------------------------------------|----------|
| W_μ^\pm | $m_W = \frac{gv}{2}$ | W^\pm |
| Z_μ | $m_Z = \frac{\sqrt{g^2 + g'^2}v}{2}$ | Z^0 |
| A_μ | $m_\gamma = 0$ | γ |
| χ | $m_\chi = \sqrt{2\lambda}v$ | Higgs |

Table 1.2: The physical fields from electroweak symmetry breaking.

The electric charge is connected to the weak mixing angle by:

$$e = g \sin \theta_W \quad (1.27)$$

The existence of the W^\pm and Z^0 bosons was confirmed experimentally by the UA1 and UA2 experiments in CERN. The masses were measured to be:

$$m_W = 80.4 \pm \text{GeV} \quad m_Z = 91.2 \pm \text{GeV} \quad (1.28)$$

The weak mixing angle, θ_W , was measured independently to satisfy $\sin \theta_W = 0.23$ in good agreement with the predictions of the electroweak theory.

Both leptons and quarks feel the weak interaction. The W^\pm interact only with left-handed fermions. Handedness (or chirality) is the eigenvalue of the γ^5 matrix. It corresponds to the helicity (the projection of the spin onto the direction of motion) in the relativistic limit $m \ll E$.

The left handed components form SU(2) doublets while the right handed components are singlets under SU(2) as in Equation 1.29 for leptons and Equation 1.30 for quarks.

$$E_L = \begin{pmatrix} e \\ \nu_e \end{pmatrix}_L \quad e_R \quad (1.29)$$

$$Q_L = \begin{pmatrix} u \\ \bar{d} \end{pmatrix}_L \quad u_R \quad \bar{d}_R \quad (1.30)$$

The Yukawa couplings are:

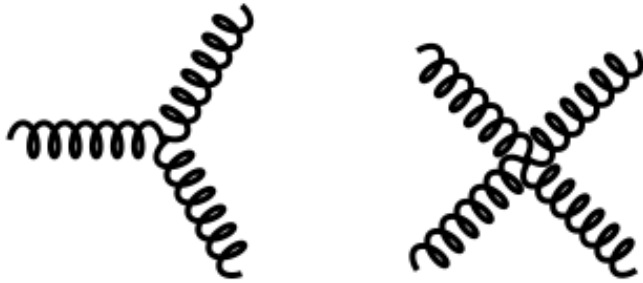


Figure 1.2: Gluon self-interactions occur because gluons carry colour charge. This is required by gauge invariance due to the non-abelian nature of SU(3).

$$L_Y = -y_e \bar{E}_L \phi e_R - y_d \bar{Q}_L \phi d_R - y_u \bar{Q}_L \phi^* u_R + h.c. \quad (1.31)$$

Quark mixing.

1.3.3 Quantum Chromodynamics (QCD)

SU(3) is the symmetry group of the strong force. Particles which interact via the strong force carry colour charge. Quarks come in 3 colours denoted r, g and b. There are 8 gluons which correspond to the 8 generators of SU(3). Gluons carry colour charge and so interact with each other. This is required by gauge invariance due to the non-abelian nature of SU(3).

The Hadron Electron Ring Accelerator (HERA) made electron proton collisions to determine the structure of the proton. Deep inelastic scattering in the ZEUS and H1 detectors revealed that the structure functions of the proton are independent of the momentum transfer, Q^2 , and dependent only on $x = \frac{Q^2}{2p \cdot q}$. This is called Bjorken scaling and lead to the parton model in which the proton is made of partons which carry a fraction, x , of the proton momentum. Figure 1.4 shows the independence of the cross-section with Q^2 over 5 orders of magnitude.

The Parton Density Functions (PDFs) are the probability distribution for the fraction of the proton momentum carried by each parton. The PDFs need to be

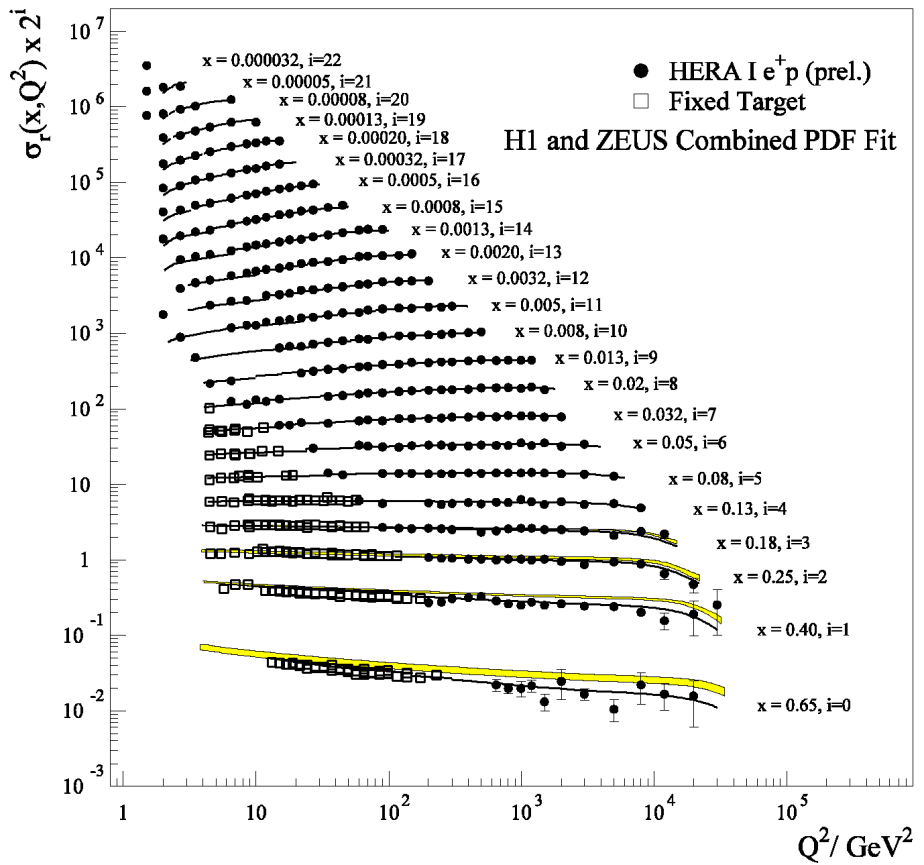


Figure 1.3: The structure functions of the proton are independent of Q^2 over 5 orders of magnitude.

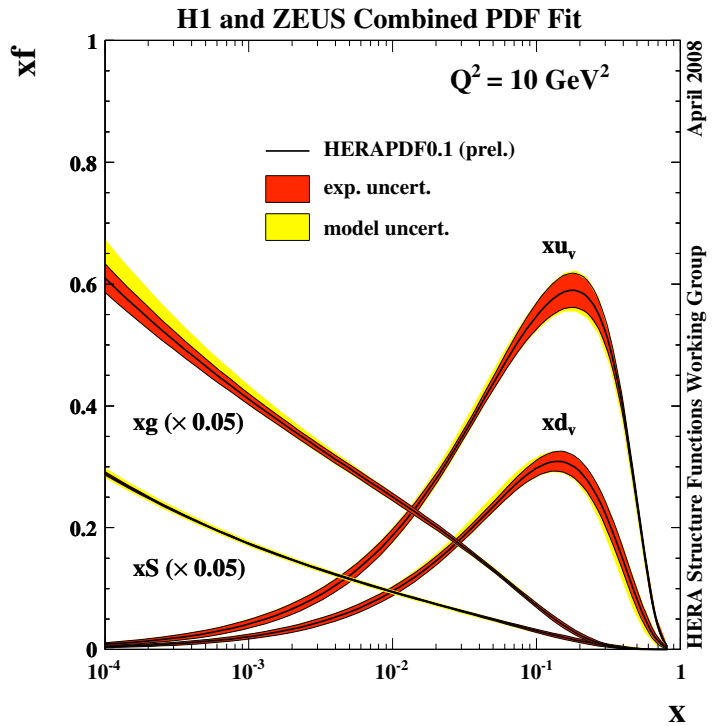


Figure 1.4: The Parton Density Functions (PDFs) measured by H1 and ZEUS.

known to make reliable Monte Carlo simulations and cross-section predictions for the LHC. Figure ?? shows the parton density functions measured by H1 and ZEUS.

The coupling strength of the strong force varies with energy. Figure 1.5 shows the variation in coupling strength of the strong, weak and electromagnetic force as a function of energy.

The strong force is strong at low energies where quarks exist only in colourless bound states. This is known as confinement. At high energies the strong force becomes weaker as the partons behave as free particles. This is known as asymptotic freedom.

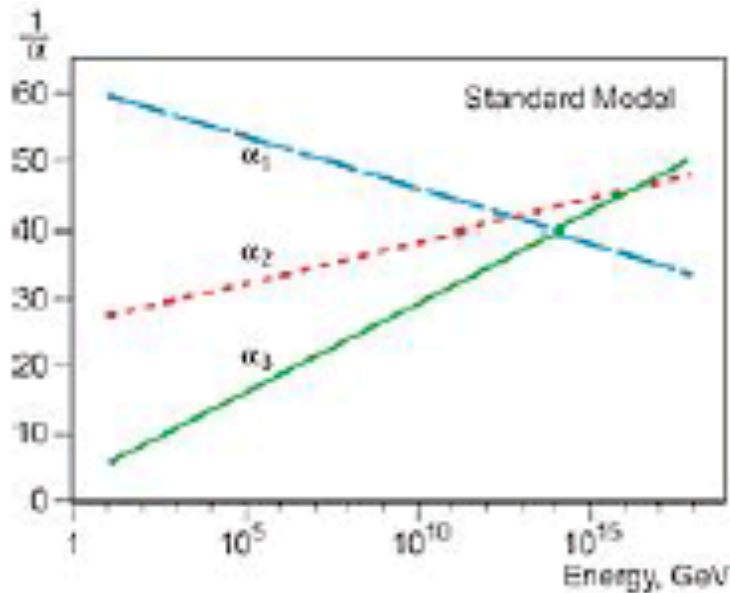


Figure 1.5: The coupling strengths of the electromagnetic force, the weak force and the strong force as a function of energy.

1.4 Motivation for new physics at the TeV scale

The motivations for expecting the discovery of new physics at the TeV scale are considered.

1.4.1 WW scattering

WW scattering (among other similar processes) has been observed at the Large Electron Positron (LEP) collider and the cross-section has been measured. Without additional couplings the interaction violates unitarity. The Higgs boson is one mechanism to mediate this interaction, but so far the Higgs has not been observed. Whatever the mechanism by which this interaction occurs it must be at the TeV energy scale.

Consider the scattering of longitudinally polarized W bosons: $W_L W_L \rightarrow W_L W_L$.

1.4.2 New energy scale

This is simply the observation that we are exploring a higher energy scale than has previously been explored so we can expect to find new things. In the same way as when explorers explore a new land they can expect to see things they have not seen before.

1.4.3 Hierarchy Problem

The hierarchy problem is fundamentally a problem of scale. There are two fundamental energy scales in physics: the Electroweak scale ($\sim 100\text{GeV}$) and the Planck scale ($\sim 10^{18}\text{GeV}$), where gravity becomes as strong as the gauge interactions. Certainly at the Planck scale the Standard Model will no longer hold because a quantum treatment of gravity is needed. The Electroweak scale is well measured at colliders and the results form our current understanding of particle physics. It could be that there is no new physics between the two scales. If we reject such a possibility, then the Higgs mass is alarmingly sensitive to any new physics.

When one-loop quantum corrections to the Higgs mass squared are calculated, there is a quadratic divergence depending on the cut-off used to do the calculation. It is worth noting that the cut-off is not peculiar to QFT. In Newtonian gravity when we calculate the gravitational potential due to the sun we neglect the mass distribution of the sun and simply consider it as a point mass for distances much larger than the radius of the sun. The problem here arises because the corrections do not give a vanishing contribution. The Higgs mass squared is divergent.

There are a number of different models for beyond the Standard Model physics which seek to address this problem including supersymmetry, extra dimensions and technicolor. In supersymmetry this is accomplished by introducing a symmetry between fermions and bosons. For every Standard Model particle there is a supersymmetric partner which is a boson for fermions and a fermion for bosons. The fermions give a -1 contribution to the Higgs mass correction while the bosons give a +1 contribution exactly cancelling each other.

1.4.4 Dark Matter candidates

Only 5% of the mass/energy in the universe is normal matter that we observe. The remainder is made up of dark matter (25%) and Dark Energy (70%). Dark energy is an unknown that is introduced to explain the expansion of the universe. Dark matter is well known.

The existence of dark matter is inferred from its gravitational interaction with normal matter. Dark matter was postulated as missing mass to account for the orbital velocities of galaxies in clusters. There have since been other observations that have confirmed the existence of dark matter including the rotational speed of galaxies and the bullet cluster.

The bullet cluster provides the best evidence yet on the nature of dark matter. It consists of two colliding clusters of galaxies. The visible matter (stars) pass straight through slowed only by gravitation. The hot gas which represents most of the normal matter is detected through X-rays. The hot gas slows more than the stars due to its electromagnetic interactions. Another piece of information comes from gravitational lensing. In the absence of dark matter the gravitational lensing is expected to follow the normal matter (i.e. the X-ray gas). However, the gravitational lensing is strongest in the separated regions around the visible matter. This provides support to the idea that most of the mass of the galaxies is made up of collisionless dark matter.

If dark matter interacts through the weak force, then it could be observed at the LHC. Dark matter may not interact weakly. Perhaps it interacts only gravitationally. Additionally it may not show up at the TeV scale. I will simply make two statements which offer some support for the discovery of possible dark matter candidates at the LHC. Firstly, TeV scale weakly interacting massive particles give dark matter abundances in the universe at about the experimentally observed level. Secondly, SUSY (which is one of the popular theories of physics beyond the standard model) predicts a set of supersymmetric particles the lightest of which could be a dark matter candidate.

1.5 Supersymmetry

Supersymmetry proposes that for every particle there is a supersymmetric partner which is a boson for fermions and a fermion for bosons [?]. Such a symmetry ensures cancellation of the divergence in the Higgs boson mass. We can write the operator Q which generates the supersymmetric transformations as Equation 1.32.

$$Q|\text{Boson}\rangle = |\text{Fermion}\rangle \quad Q|\text{Fermion}\rangle = |\text{Boson}\rangle \quad (1.32)$$

A straightforward implementation of supersymmetry would predict a whole new set of particles with the same mass and same interactions as the Standard Model particles. Since we do not observe these particles SUSY, if it exists, must be broken. The superpartners can then be at a higher mass scale. There are various different schemes for SUSY breaking (ref). Here only Gauge Mediated SUSY Breaking (GMSB) is considered.

1.6 Strong production Gauge Mediated SUSY breaking

Squark and gluino production GMSB has a low production cross section at low centre of mass energy. It was inaccessible at the Tevatron ($\sqrt{s} = 1.96\text{TeV}$). However CDF and D0 were able to place limits on electroweak production GMSB. At the LHC, the higher centre of mass energy ($\sqrt{s} = 7\text{TeV}$) means that strong production GMSB is accessible.

squark mass vs gluino mass phase space

Strong production GMSB events must contain at least two jets from the two squarks/gluinos. Assuming R-parity conservation, the decays of the squark and gluino are fixed. Squarks decay to a quark and the next particle in the SUSY mass hierarchy ($\tilde{q} \rightarrow q\tilde{X}$) resulting in one jet. Gluinos decay to a quark anti-quark pair and the next particle in the SUSY mass hierarchy ($\tilde{g} \rightarrow q\bar{q}\tilde{X}$) resulting in two jets. Thus the mass of the squark relative to the gluino indicates

how many jets we expect from the SUSY events. With a high squark mass the gluinos are produced more and so 4 jets are expected, but with a high gluino mass the squarks are produced more and so only 2 jets are expected.

SUSY events contain real ME_T from the Lightest Supersymmetric Particle (LSP). In GMSB, the lightest SUSY particle is the Gravitino (\tilde{G}) and the Next Lightest Supersymmetric Particle (NLSP) is the Neutralino ($\tilde{\chi}^0$). The Neutralino decays into a photon and a Gravitino $\tilde{\chi}^0 \rightarrow \gamma \tilde{G}$. Since the two photons and the two Gravitinos (sources of ME_T) come from separate decay chains there is no special relationship between the two. They do not have a particular invariant mass nor a particular angular separation. The ME_T distribution is very broad and the photons are independent.

Chapter 2

CMS Detector and Reconstruction

2.1 Introduction

The LHC is a 27km circular particle accelerator which lies across the French-Swiss border about 100m underground. It was designed to accelerate and collide beams of protons or heavy ions. The design centre of mass energy (\sqrt{s}) for proton-proton collisions is 14TeV. The design luminosity is $10^{34}\text{cm}^{-2}\text{s}^{-1}$. The LHC is the highest energy particle accelerator ever built.

Figure 2.1 shows a diagram of the LHC accelerator complex. Protons are extracted from a cylinder of hydrogen gas and accelerated first by a linear accelerator which injects them into the Proton Synchrotron (PS), which accelerates them to 25GeV and feeds the Super Proton Synchrotron (SPS). The SPS accelerates the beams to 450GeV and subsequently injects them into the LHC.

The CMS detector is one of the four general purpose LHC experiments. It was designed to explore O(TeV) energy proton-proton collisions for indications of physics beyond the Standard Model. The CMS detector is 21.6m long and 14.6m in diameter and has a total weight of 13 500 tonnes. It is located at Point 5 on the LHC ring near Cessy in France. Figure 2.2 shows the layout of the

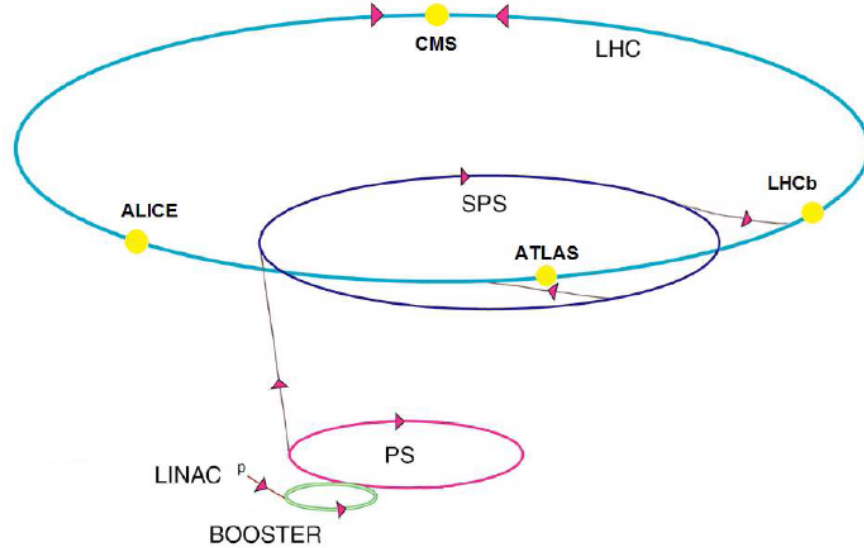


Figure 2.1: A diagram of the LHC accelerator complex. Reproduced from [4].

CMS detector.

In the following sections each component of the CMS detector is described starting from the innermost and going to the outermost. The CMS trigger and the computing model are also described.

2.2 Pixel Detector

The pixel detector consists of 3 barrel layers with 2 endcap disks on each side (Figure 2.3). The barrel layers are at mean radii of 4.4cm, 7.3cm and 10.2cm and have a length of 53cm. The endcap disks are placed either side at $|z| = 34.5\text{cm}$ and 46.5cm .

The purpose of the pixel detector is to give good primary vertex resolution and to initiate track reconstruction. The pixel size is $100 \times 150\mu\text{m}$. The spatial resolution is about $10\mu\text{m}$ for the (r,ϕ) measurement and about $20\mu\text{m}$ for the z measurement.

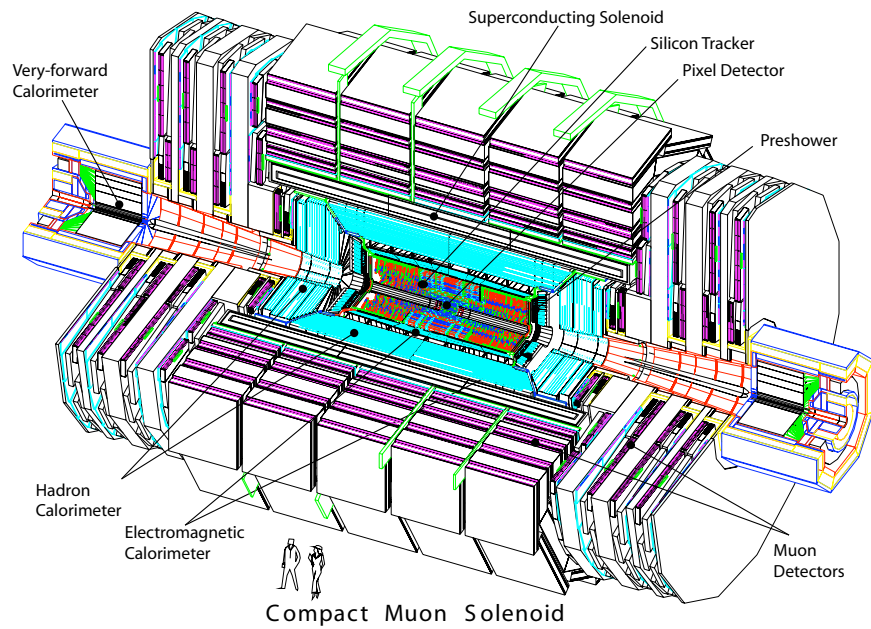


Figure 2.2: A view of the layers inside the CMS detector. Reproduced from [4].

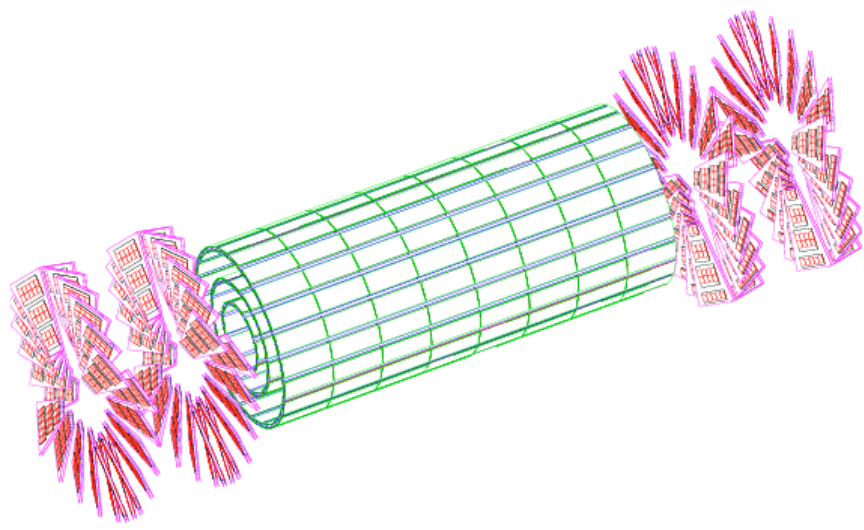


Figure 2.3: A diagram of the pixel detector. Reproduced from [4].

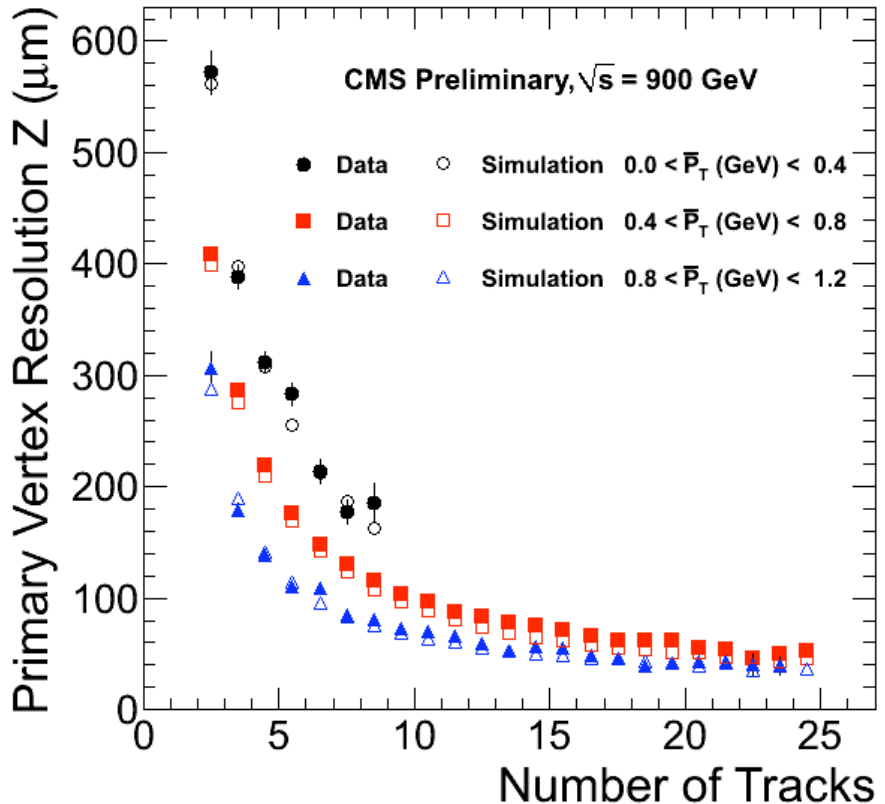


Figure 2.4: The Primary Vertex resolution as a function of the number of tracks for various average track p_T ranges. Reproduced from [13].

The primary vertex is found by clustering selected tracks in z . A fit is performed based on a weight assigned to each track which is between 0 and 1 depending on the compatibility with the vertex [13].

The primary vertex resolution depends strongly on the number of tracks in the fit. Figure 2.4 shows the primary vertex resolution as a function of the number of tracks for various average track p_T ranges.

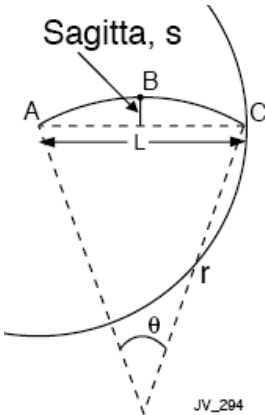


Figure 2.5: Diagram illustrating how the transverse momentum is calculated from the curvature of the track in the magnetic field.

2.3 Silicon Strip Tracker

The silicon strip tracker is designed to measure the trajectory of charged particles. It is made from strips of silicon which charged particles ionise. The technology is the pn junction with a reverse bias voltage applied, which creates a depletion region. Charged particles ionise inside the depleted region creating electron hole pairs which travel to the electrodes where they form a signal. Silicon is used because it produces fast, radiation hard electronics and good resolution.

The transverse momentum of a particle is measured from the curvature of the track in the magnetic field by Equation 2.1, where p_T is the transverse momentum in GeV, B is the magnetic field in Tesla and r is the radius of curvature in metres. Only the hits are measured directly. The “sagitta” or distance s in Figure 2.5 is deduced and the transverse momentum is calculated from this. Since s is inversely proportional to p_T , the resolution is worse at higher p_T .

$$p_T = 0.3Br \quad (2.1)$$

The silicon strip tracker is made up of 4 sub-detectors: the Tracker Inner Barrel (TIB), the Tracker Outer Barrel (TOB), the Tracker Endcap (TEC) and the

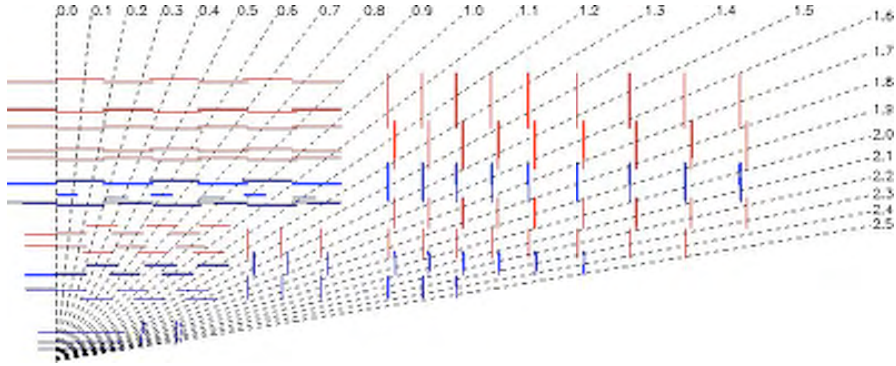


Figure 2.6: The layout of the silicon strip tracker. Reproduced from [4].

Tracker Inner Disks (TID). Figure 2.6 shows the layout of the tracker.

The resolution of the tracker is shown for muons of $p_T = 1, 10$ and 100 GeV in Figure 2.7.

2.4 Electromagnetic Calorimeter

The Electromagnetic Calorimeter (ECAL) is designed to measure the energy of electromagnetic showers from photons, electrons and π^0 s. It must provide good energy resolution and good containment of the electromagnetic shower.

The ECAL has 3 components: the ECAL barrel (EB), the ECAL endcap (EE) and the ECAL pre-shower (ES). The EB covers the range $|\eta| < 1.479$. The EB radius is 1.29m and the total length in the z-direction is 6m. The EE consists of two identical detectors on either side of the EB covering the region $1.479 < |\eta| < 3$. The ES is positioned in front of the EE to improve the γ/π^0 discrimination which is important for $H \rightarrow \gamma\gamma$ searches. Figure 2.8 shows a diagram of the layout of the ECAL.

An electromagnetic shower progresses through two processes **bremsstrahlung**, where an electron or positron emits a photon, and **pair production**, where a photon converts to an electron and a positron. Figure 2.9 shows how an electromagnetic shower progresses. The shower continues until the electrons/photons

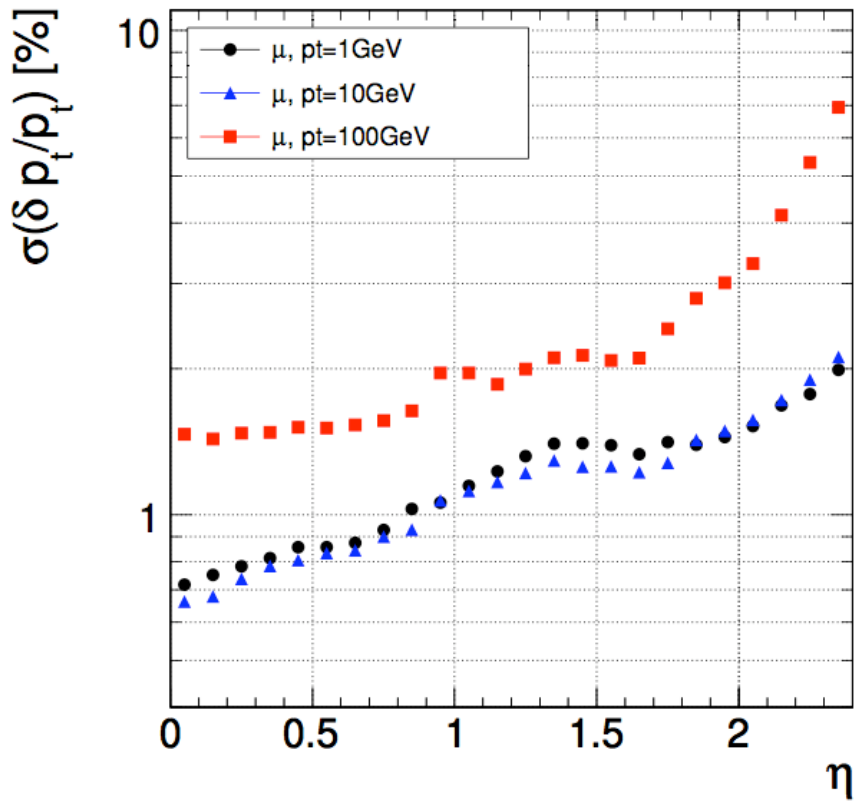


Figure 2.7: The resolution of the tracker as a function of η for muons of $p_T = 1$, 10 and 100 GeV.

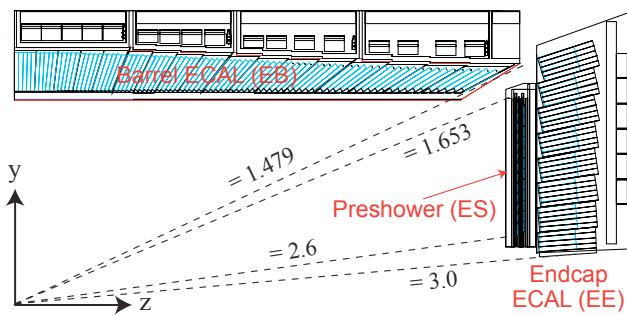


Figure 2.8: A diagram of the layout of the ECAL.

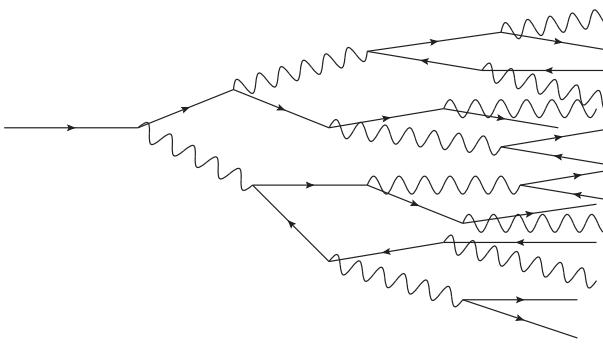


Figure 2.9: An illustration of the development of an EM shower.

reach a critical energy, E_c , where no more particles are produced as the dominant energy losses are through Compton scattering and photoelectric effect for photons and ionisation for electrons.

The calorimeter measures the energy. have a heavy material that initiates the shower and a scintillation material which converts it to a light signal. Sampling calorimeters are in layers with layers of heavy material to initiate the shower and layers of scintillator to sample the shower. In homogeneous calorimeters the heavy material and the scintillator are one and the same. Materials have two characteristic lengths which describe the shape of EM showers. Radiation length is the length over which an electron or photon's energy is reduced to $1/e$ of its initial energy. Moliere radius describes the lateral size of the shower; it is the radius which contains 90% of the energy of the shower.

The EB and EE are homogeneous calorimeters made of lead tungstate ($PbWO_4$) crystals. This material was chosen because of its short radiation length ($X_0 = 0.89\text{cm}$) and short Moliere radius ($r_m = 2.2\text{cm}$). The crystals have a low light yield. The scintillation light is blue/green with a maximum at $420 - 430\text{nm}$. The light is detected by Avalanche Photodiodes (APDs) in the EB and Vacuum Phototriodes (VPTs) in the EE. The choice of photodetectors was based on the requirement of adequate electronic gain given the low light yield of the crystals, operation in the magnetic field and radiation tolerance for the environment in

which they operate.

In the EB the length of the crystals is 23cm ($26 X_0$) and the cross-section is 0.0147×0.0147 in $\eta\text{-}\phi$ or about 22mm \times 22mm at the front face. Figure 2.8 shows the layout of crystals in the EB. The crystals are angled at 3° with respect to the interaction point. To minimise the risk of particles escaping down the cracks between the crystals. The ECAL is divided into regions called Trigger Towers (TTs) for which trigger primitives (crystal energy sums) used by the trigger are calculated. There are 85×72 TTs in the EB each consisting of 5x5 arrays of crystals.

In the EE the length of the crystals is 22cm ($25X_0$). Due to the geometry of the detector the granularity in $\eta\text{-}\phi$ varies across the EE.

The ES is a sampling calorimeter made of lead to initiate the shower and silicon strip sensors to sample the shower. It has a depth of 20cm ($3X_0$).

The energy resolution, σ , has been parameterised as a function of energy in Equation 2.2.

$$\left(\frac{\sigma}{E}\right)^2 = \left(\frac{S}{\sqrt{E}}\right)^2 + \left(\frac{N}{E}\right)^2 + C \quad (2.2)$$

The parameters S, N and C represent the stochastic term, the noise term and the constant term respectively.

The stochastic term, $\frac{S}{\sqrt{E}}$, is related to the uncertainty in the number of photons detected. The number of photons for a given energy electromagnetic shower follows a Poisson distribution. So if N photons are detected, the uncertainty is \sqrt{N} . And the energy is proportional to the number of photons, hence the \sqrt{E} dependence of this term.

The noise term, $\frac{N}{E}$, is not energy dependent. The noise is about 20MeV per crystal, or 100MeV per trigger tower.

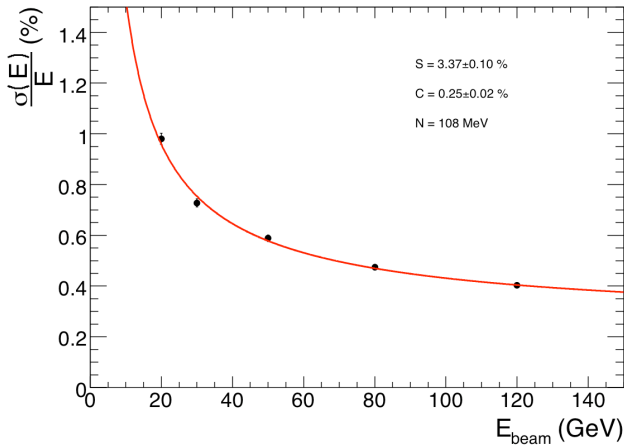


Figure 2.10: The energy resolution of the ECAL as a function of the beam energy as measured using the test beam. The parameterisation of the resolution has been fitted and values extracted for the parameters. Reproduced from [3].

The constant term, C , contains those uncertainties which are proportional to energy such as inter-calibration uncertainties.

Figure 2.10 shows the energy resolution of the ECAL as a function of beam energy measured using the test beam [3].

2.5 Hadronic Calorimeter

The Hadronic Calorimeter (HCAL) measures the energy of hadronic showers and assists in the triggering and measurement of jets and missing transverse energy.

The HCAL covers the range $|\eta| < 5$ and consists of four subdetectors: the Hadron Barrel (HB), the Hadron Outer (HO), the Hadron Endcap (HE) and the Hadron Forward (HF). The HB covers the region $|\eta| < 1.4$ and contains towers with a granularity of $\Delta\eta \times \Delta\phi = 0.087 \times 0.087$. The HB is constrained radially to be between the ECAL outer surface (at $r = 1.77\text{m}$) and the inner surface of the solenoid (at $r = 2.95\text{m}$). This constrains the amount of material that can be put

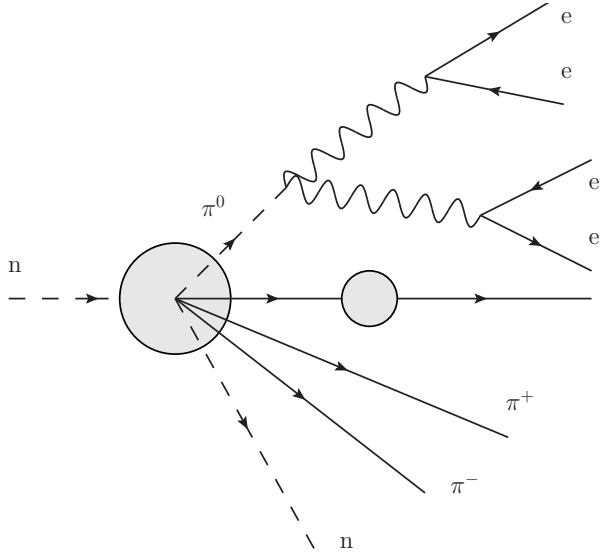


Figure 2.11: An illustration of the development of a hadronic shower.

in to absorb the hadronic showers. For this reason the HO lies outside the HB and the magnet in the region $|\eta| < 1.26$ and contains extra scintillators to catch energy leakage from high energy jets. The HE covers the range $1.3 < |\eta| < 3.0$ with a granularity that varies with η from $\Delta\eta \times \Delta\phi = 0.087 \times 0.087$ at $\eta = 1.3$ to $\Delta\eta \times \Delta\phi = 0.350 \times 0.174$ at $\eta = 3.0$. The region $3 < |\eta| < 5$ is covered by the HF.

The HCAL is a sampling calorimeter with brass absorbers and plastic scintillator tiles in the central and endcap regions and steel absorbers with quartz fibre scintillators in the forward region. Brass has a short interaction length () providing adequate containment within the limited space inside the magnet. Steel is used in the forward region due to its greater radiation tolerance. The scintillation light is detected by multi-channel hybrid photodiodes (HPDs) in the central region and photomultiplier tubes (PMTs) in the forward region.

Figure 2.11 shows a diagram of the development of a hadronic shower.

The jet energy resolution and the missing transverse energy resolution are the key indicators of the performance of the HCAL. Figure 2.12 shows the jet trans-

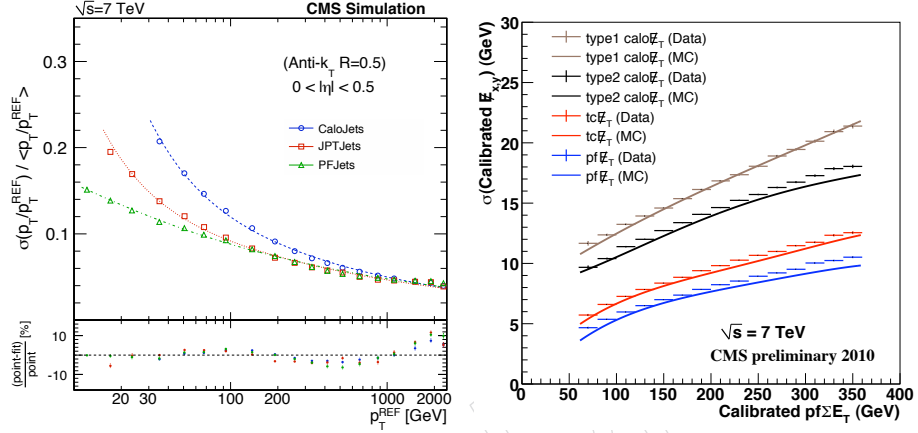


Figure 2.12: Performance measures for the HCAL: (a) the jet p_T resolution as a function of jet p_T for various different jet reconstructions and (b) the ME_T resolution as a function of Sum E_T for different ME_T reconstructions. Reproduced from [9, 10].

verse energy resolution and the missing transverse energy resolution [9, 10].

2.6 Superconducting Solenoid Magnet

The superconducting solenoid generates a uniform 3.8T magnetic field. The magnetic field is important for determining the charge of particles and for the momentum measurement of charged particles, particularly low momentum charged particles and muons. The solenoid is 12.5m in length and 6m in diameter. The flux is returned through an iron yoke to provide a magnetic field which bends muons in the opposite direction. The iron is in layers between the muon chambers.

The precision of the momentum measurements in the inner tracker relies on a homogeneous magnetic field. Within the tracker the magnetic field is homogeneous to within 5% [14] and has been mapped with a precision better than 0.1% [6].

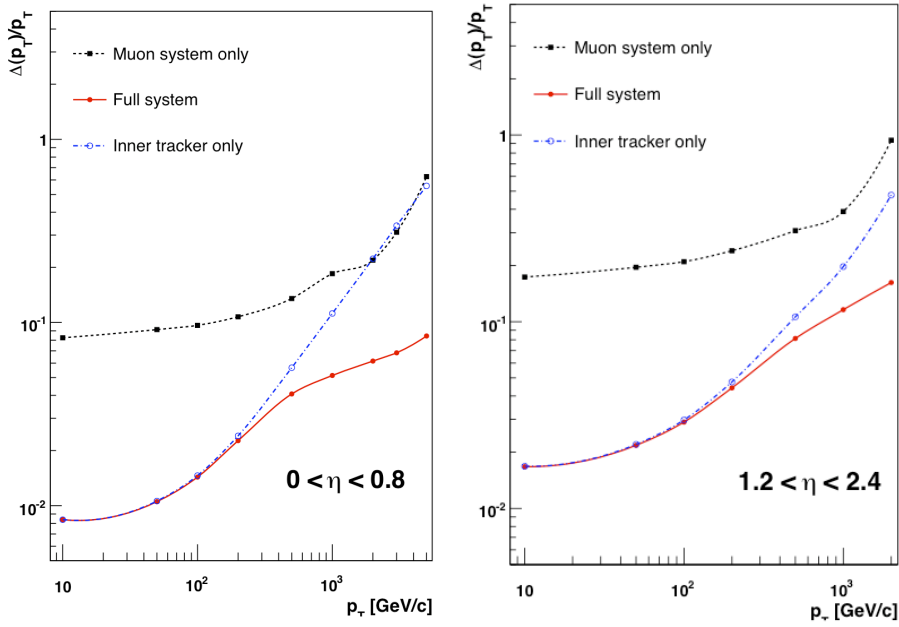


Figure 2.13: The muon p_T resolution as a function of muon p_T for (a) $\eta < 0.8$ and (b) $1.2 < \eta < 2.4$. Reproduced from [5].

2.7 Muon System

The purpose of the muon system is the identification and triggering of muons. It also provides a momentum measurement of the muons.

The muon system has a barrel region in the pseudorapidity range $\eta < 1.2$ and two endcaps with $1.2 < \eta < 2.4$. Standard drift tube chambers are used in the barrel and cathode strip chambers in the endcaps. The muon ionises the gas as it passes through the chamber. The resolution increases with the p_T of the muon since the straighter the track the more difficult it is to accurately determine the curvature. Also the resolution is worse in the endcaps where the fake rate is higher and the magnetic field is less uniform. Figure 2.13 shows the muon p_T resolution as a function of muon p_T .

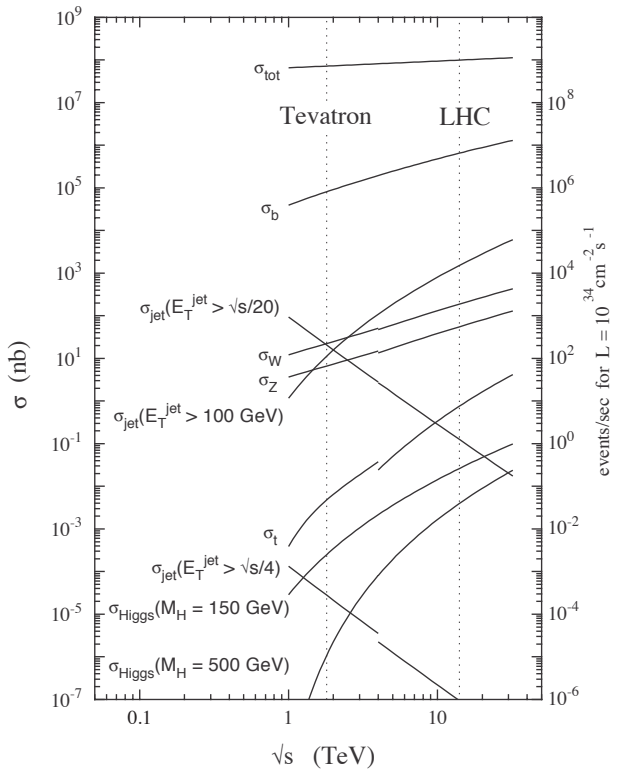


Figure 2.14: The cross-sections of various processes as a function of centre-of-mass energy.

2.8 Trigger

With a soft QCD cross-section of $\sim 1\text{mb}$ and a luminosity of $10^{33}\text{cm}^{-1}s^{-1}$ ($1\text{nb}^{-1}s^{-1}$) the event rate is $\sim 1 \text{MHz}$. However, most of these are uninteresting soft QCD events. Interesting events such as W/Z production, Higgs production or SUSY events have much smaller cross-sections. Figure 2.14 shows the cross sections of various processes. Also there is a technical limit on the rate at which data can be read out. The CMS data acquisition (DAQ) bandwidth limits the event rate to $\sim 100\text{kHz}$. Offline reconstruction and storage facilities further limit the rate to $\sim 100\text{Hz}$. The goal of the trigger is to select the interesting events to read out and process.

There are two components to the trigger: Level 1 and HLT. Level 1 consists of on-detector hardware and the goal is to reduce the rate to $\sim 10\text{kHz}$ to satisfy the constraint set by the DAQ bandwidth. The HLT is run on a farm of computers in a room above the CMS detector. It reconstructs physics objects and makes decisions based on the presence and quality of these to further reduce the rate to $\sim 100\text{Hz}$ to satisfy the constraint set by the storage and reconstruction facilities.

2.9 CMS Computing Model

CMS has produced $O(100\text{PB})$ of data and the quantity is growing. No single computer centre is capable of handling such a large quantity of data. The CMS computing model involves a network of data centres across the world (Figure 2.15) in a hierarchy of Tiers.

- Tier 0 is the data centre at CERN which is directly connected to the experiment. It stores the RAW data and produces the first reconstruction which is subsequently transferred to Tier 1 sites.
- Data from Tier 0 is distributed to 8 Tier 1 sites. Each Tier 1 site is responsible for storing a second copy of the RAW and reconstructed data. A lot of reprocessed data is also stored at the Tier 1 sites.
- Data from the Tier 1 sites is transferred to 38 Tier 2 sites. These data centres store data for analysis by CMS physicists. Data at the Tier 2 sites is not complete and is not stored permanently, but is updated based on the requirements of the CMS collaboration.

2.10 Photon Reconstruction

??

Photons make electromagnetic showers in the ECAL. Electromagnetic showers are reconstructed from the energy deposits in the ECAL crystals. The clustering algorithm starts with the energy deposits in single crystals and groups these together starting with the highest energy crystal. A strip 5 crystals wide in the η direction and with dynamic ϕ length is used to contain the energy in the



Figure 2.15: A map showing the geographical distribution of CMS Tier 1 (red dots) and Tier 2 (blue dots) data centres. Reproduced from [1].

cluster or clusters. To incorporate bremsstrahlung from electrons, the strip can be extended in the ϕ direction. A description of the superclustering algorithm is given here [11].

Fake photons from QCD come from jets and so tend to have plenty of activity in the surrounding detectors. In contrast, prompt photons tend to be isolated with little surrounding activity. Isolation is one of the variables used to select photons because of its background rejection power. There are three independent isolation measures based on the ECAL, the HCAL and the tracker.

Fake photons from jets also tend to have a hadronic component as well as an electromagnetic component while prompt photons are purely electromagnetic. Electromagnetic showers have a particular shower shape. Prompt photons can be distinguished from fakes by the shower shape. Photons are distinguished from electrons by the tracker. Electrons, being charged particles, ionise in the silicon tracker and so leave a track. Photons do not.

Based on these considerations, there are six variables used for the photon selection:

- **ECAL isolation** is defined as the sum of the energy deposited in the crystals of the ECAL in a $\Delta R = 0.4$ circle around the photon. A smaller circle of $\Delta R = 0.1$ around the photon is excluded from the isolation sum to avoid counting the photon itself in the isolation. Also a strip along ϕ of width $\Delta\eta = 0.04$ is excluded from the isolation sum to avoid including bremsstrahlung from electrons.
- **HCAL isolation** is defined as the sum of the energy deposited in the HCAL towers in a $\Delta R = 0.4$ circle around the photon position. A smaller circle of $\Delta R = 0.1$ is excluded from the isolation sum to avoid counting rear-leakage from high energy photons in the isolation.
- **Track isolation** is defined as the sum of the p_T of tracks inside a cone of $\Delta R = 0.4$ around the photon and toward the primary vertex. A hollow cone is used $\Delta R < 0.1$ is excluded from the isolation sum.
- **H/E** is the ratio of the hadronic energy deposited in the HCAL behind the photon to the photon energy. Jets faking photons are likely to have a significant amount of hadronic energy while for prompt photons the amount of hadronic energy is likely to be small.
- **Shower Shape** ($\sigma_{i\eta i\eta}$). The width of the shower in the η direction is used as a measure of the shower shape. The η direction rather than the ϕ direction is used because bremsstrahlung can cause electromagnetic showers to be spread out in ϕ . $\sigma_{\eta\eta}$ is the r.m.s width of the shower in the η direction. The variable used here is $\sigma_{i\eta i\eta}$, which calculates the width in terms of number of crystals in the η direction rather than η itself. This is better because it does not count the gaps between crystals (where there is no showering) in the width and it is not distorted by the geometry of the detector in the end-cap region.
- **Pixel Seed.** A pixel seed is a track stub in the pixel detector that is the first step in track reconstruction. The photon selection requires that there is no pixel seed corresponding to the electromagnetic shower.

2.11 Jet Reconstruction

Jets are collimated bunches of stable hadrons originating from partons (quarks and gluons) after fragmentation and hadronisation. Jets are reconstructed using the anti-KT algorithm with a cone size of 0.5. The anti-KT algorihtm is a sequential clustering algorithm which is IR safe and produces circular cone-shaped jets. The anti-KT algorithm is used because it has a higher efficiency, lower fake rate and is less sensitive to pile-up than the other algorithms.

The reconstruction uses so-called “particle flow” objects (including photons, charged hadrons and neutral hadrons) as input. The philosophy of the particle flow reconstruction is to have a complete and consistent event hypothesis. All components of the detector are used in the reconstruction. Particle flow jets have better resolution than other jet reconstructions (see Figure 2.12).

Chapter 3

Data, Trigger and Event Selection

3.1 Data

Since March 2011 CMS has been taking proton-proton collisions data at 7TeV centre of mass energy. A higher centre of mass energy increases the production cross-section of certain processes, for example strong production SUSY, and also enables the production of more massive particles. It should be noted that the important energy is not the centre of mass energy of the proton collision, but that of the parton collision which is $\sim 1\text{TeV}$ on average.

The luminosity has increased over time. As the integrated luminosity increases more data are available to improve the significance of observations and the accuracy of measurements. The luminosity has been increased by increasing the intensity of the beams and the number of bunches. Increasing the intensity of the beams leads to more interactions per bunch crossing – an effect called pile-up. During the period when this data was taken the luminosity was $\sim 10^{33}\text{cm}^{-2}\text{s}^{-1}$.

Figure 3.1 shows the integrated luminosity recorded by CMS over time until September 2011.

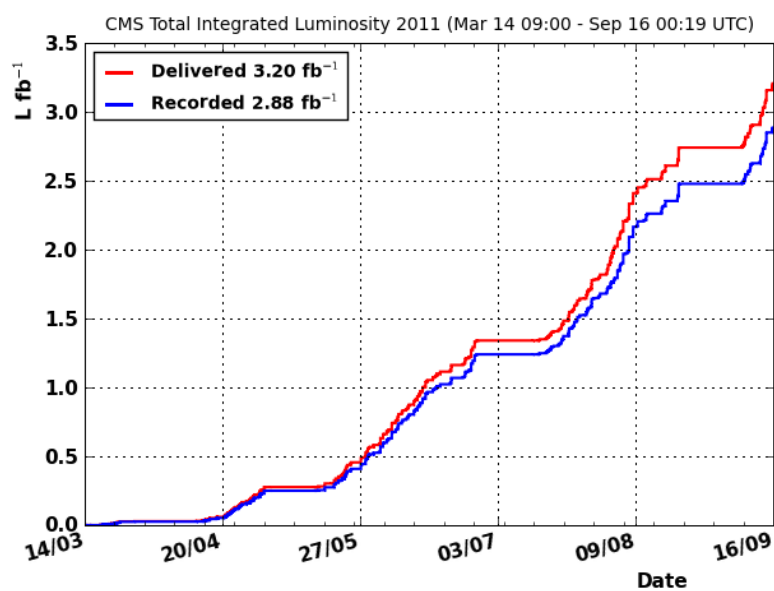


Figure 3.1: The integrated luminosity vs time delivered to (red) and recorded by (blue) CMS during stable beams at $\sqrt{s} = 7\text{TeV}$.

This analysis uses 1.1fb^{-1} of data at $\sqrt{s} = 7\text{TeV}$ taken from March to June 2011. This corresponds to the data set used for the International Europhysics Conference in High Energy Physics in July 2011. Only data certified by the physics validation team is included in the data set. The data set contains the following:

- /PhotonHad/Run2011A-May10ReReco-v1/AOD
- /PhotonHad/Run2011A-PromptReco-v4/AOD
- /PhotonHad/Run2011A-PromptReco-v5/AOD

The data is split into Primary Datasets each with different trigger requirements. PhotonHad is one such Primary Dataset.

The software version used to reconstruct the data is CMSSW_4_2_3_patch2. CMSSW is the standard CMS reconstruction software. The reconstruction involves building jets, electrons, photons and other physics objects form the raw energy deposits in the detector.

3.2 Monte Carlo Samples

The Monte Carlo samples used in this analysis are listed in Appendix A. The Monte Carlo samples are generated using Pythia 6 [20] or Madgraph [15] with Tune Z2 (based on CTECQ6 parton distribution functions [18]). GEANT [19] is used for the detector simulation.

Pile-up is simulated in the Monte Carlo samples however the MC does not reproduce the vertex mutiplicity distribution seen in the data. To correctly simulate pile-up the MC is re-weighted to reproduce the number of vertices distribution seen in the data. Figure 3.2 shows the distribution of number of vertices in the data and MC. Figure 3.3 shows the number of vertices distribution in the MC after reweighting compared to the data to show that the correct distribution has been produced. Table 3.1 gives the re-weighting factors for each number of vertices.

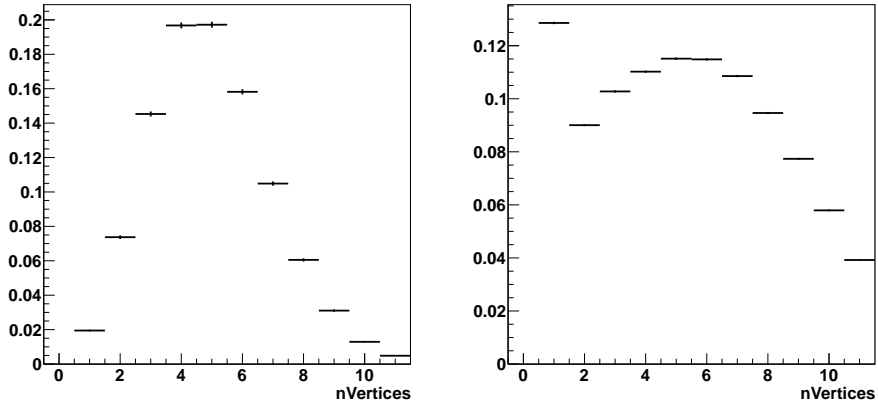


Figure 3.2: The distribution of number of vertices in the data (left) and the MC (right).

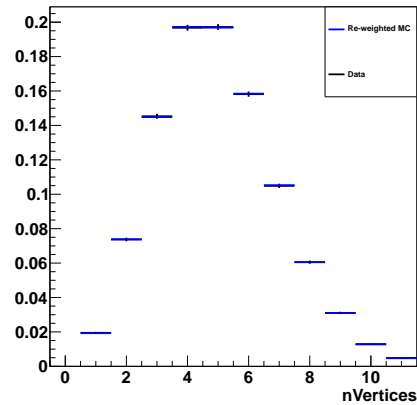


Figure 3.3: The distribution of number of vertices in the MC after reweighting (blue) compared to the data (black).

| nVertices | 1 | 2 | 3 | 4 | 5 | 6 | 7 | 8 | 9 | 10 | 11 | 12 |
|-----------|------|------|------|------|------|------|------|------|------|------|------|------|
| Weight | 0.15 | 0.82 | 1.41 | 1.79 | 1.71 | 1.38 | 0.97 | 0.64 | 0.40 | 0.22 | 0.12 | 0.04 |

Table 3.1: Re-weighting factors to be applied to the MC to correctly reproduce the number of vertices distribution in the data.

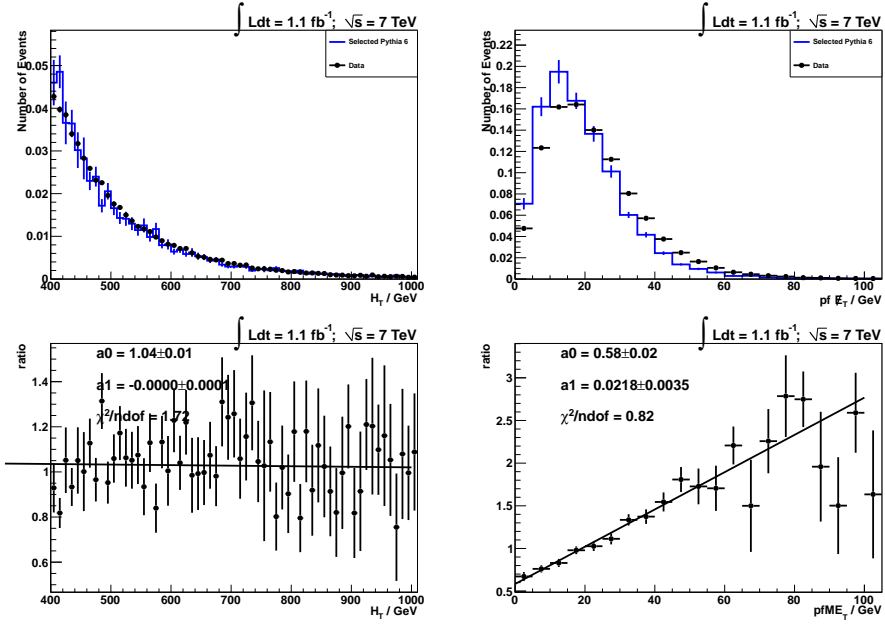


Figure 3.4: Plots of H_T and MET in data and Monte Carlo to show how accurately the Monte Carlo models the data. Ratio plots of data/MC are shown below.

Figure 3.4 shows plots of a few key variables to show how accurately the Monte Carlo models the data. The Monte Carlo prediction is good for H_T , but the ME_T distribution is not accurately predicted by the Monte Carlo.

Since the background estimation (see Section 4.2) is largely data-driven the dependence of the result on Monte Carlo is limited.

3.3 Trigger

With a soft QCD cross-section of $\sim 1\text{mb}$ and a luminosity of $\sim 10^{33}\text{cm}^{-2}\text{s}^{-1}$ ($1\text{nb}^{-1}\text{s}^{-1}$) the event rate is $\sim 10^6\text{Hz}$. Most of these are uninteresting events and the DAQ bandwidth limits the rate at which data can be read out. The goal of the trigger is to select the interesting events to read out.

There are two components to the trigger: Level 1 and HLT. The Level 1 trigger

| | L1 seed | Rate at $10^{33}\text{cm}^{-2}\text{s}^{-1}$ |
|----------------------------|---------------|--|
| HLT_Photon60_CaloIdL_HT200 | L1_SingleEG20 | (pre-scaled) |
| HLT_Photon70_CaloIdL_HT200 | L1_SingleEG20 | (pre-scaled) |
| HLT_Photon70_CaloIdL_HT300 | L1_SingleEG20 | 4Hz |
| HLT_Photon70_CaloIdL_HT350 | L1_SingleEG20 | 2.5Hz |

Table 3.2: A table of the photon and H_T triggers available in the 2011 data along with the corresponding L1 seed and rate at $10^{33}\text{cm}^{-2}\text{s}^{-1}$.

sits in a cavern next to the CMS detector. It takes “trigger primitives” such as crystal energy sums calculated by on-detector hardware which are transferred by optical link from the CMS detector. The goal is to reduce the rate to $\sim 10\text{kHz}$. Those events which pass the Level 1 trigger are fully read out and unpacked by the HLT. The HLT is run on a farm of computers in a room above the CMS detector. It reconstructs physics objects and makes decisions based on the presence and quality of these to further reduce the rate to $\sim 200\text{Hz}$.

Based on the properties of strong production GMSB, a photon + H_T trigger is ideal for this search. Table 3.2 shows a list of all the photon + H_T triggers in the 2011 data with the corresponding L1 seed and the rate at $10^{33}\text{cm}^{-2}\text{s}^{-1}$.

As the luminosity has increased more stringent trigger requirements have been necessary to keep the data rate manageable. If the rate of a trigger becomes too high, the trigger must be pre-scaled. This means that only every nth event which fires the trigger is read out where n is the prescale factor. Figure 3.5 shows the run ranges over which the various photon and jet triggers are in the trigger menu and when they become pre-scaled.

The efficiency of a trigger is evaluated with respect to a lower threshold trigger. Data ranges are selected such that the two triggers are both in the menu and both unprescaled. The triggers, A and B, are identical except that B has a higher threshold in variable x than A. To find out the efficiency of B:

1. Select events that pass A.

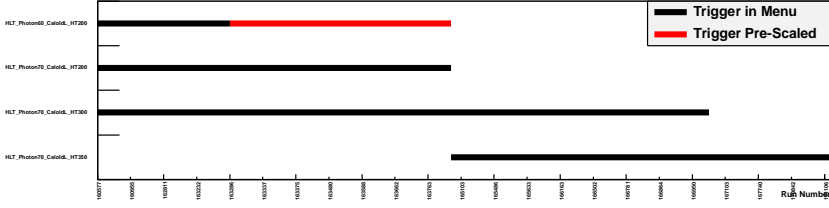


Figure 3.5: The run range over which photon and jet triggers are in the menu and when they are pre-scaled.

2. Plot the distribution of x to get histogram h_A .
3. Select events that also pass B .
4. Plot the distribution of x in these events to get histogram h_B .
5. Divide h_B by h_A , bin-by-bin to get the efficiency vs x .

In this case the variable x is H_T or photon p_T . The efficiency curve tells us where to put the off-line cut in x such that the trigger is fully efficient.

The efficiency is determined over the run ranges where the trigger overlaps with one of a lower threshold (see Figure 3.5). Figure 3.6 shows the trigger efficiency against H_T and photon p_T .

3.4 Photon Selection

Photons are selected based on variables such as isolation and shower shape which are designed to select prompt photons over fakes from jets. The photon reconstruction is described in detail in Section ???. The cut values on each of the photon selection variables are listed in Table 3.3.

3.5 Jet Selection

Jets are reconstructed based on energy deposits in the detector using the Anti-KT jet algorithm with a cone size of $\Delta R = 0.5$. The Anti-KT jet algorithm is a clustering, cone algorithm which does not suffer from the problem of infra

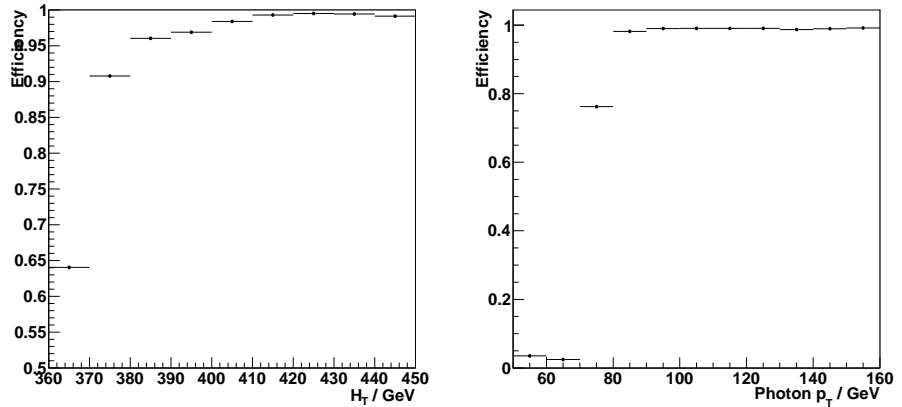


Figure 3.6: The trigger efficiency vs H_T (left) and vs photon p_T (right) relative to a lower threshold trigger.

| | |
|-----------------|-------------------|
| ECAL isolation | $4.2 + 0.006p_T$ |
| HCAL isolation | $2.2 + 0.0025p_T$ |
| Track isolation | $2.0 + 0.001p_T$ |
| H/E | 0.05 |
| Shower Shape | 0.013 |
| No Pixel Seed | True |

Table 3.3: The photon selection cuts.

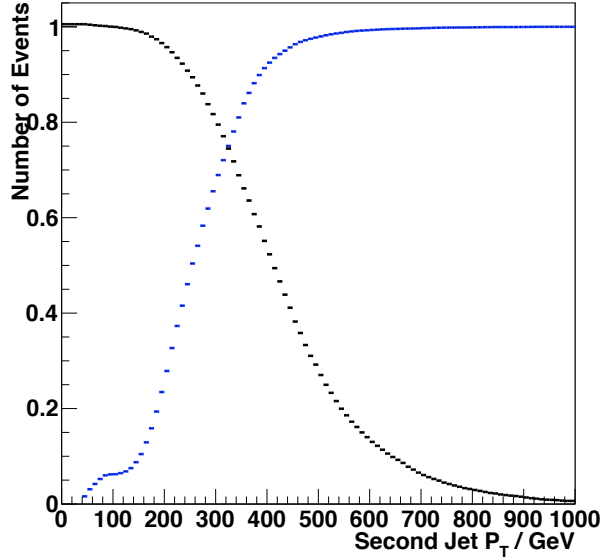


Figure 3.7: A plot of the efficiency of the signal (black) and the background rejection (blue) as a function of the jet p_T threshold.

red and collinear divergences. The Anti-KT algorithm is the most widely used within CMS because it has higher efficiency than the other algorithms.

Under the anti-KT algorithm energy deposits are clustered together within a cone according to their distance from each other. The “distance”, d_{ij} , between objects (energy deposits/particles) is defined by Equation 3.1.

$$d_{ij} = \min(p_{T1}^{-2}, p_{T2}^{-2}) \frac{\Delta_{ij}}{R} \quad (3.1)$$

$\Delta_{ij} = \sqrt{\Delta\eta^2 + \Delta\phi^2}$ and R is the radius of the cone.

Two jets with $p_T > 80\text{GeV}$ and $|\eta| < 2.5$ are required. The η threshold corresponds to the tracker boundary. The p_T threshold should be chosen as high as possible to reject background, but with the signal efficiency close to 100%. Figure 3.7 shows the signal efficiency and the background rejection as a function of the jet p_T threshold.

3.6 Missing Transverse Energy

By conservation of momentum, the sum of the momenta of all the final state particles in a collision is equal to the sum of the momenta of all the initial state particles. The initial longitudinal momentum of the colliding partons is unknown since the fraction of the proton momentum that each parton carries is unknown for any individual event. However, the initial transverse momentum is known to be zero so the final transverse momentum must also be to zero.

Events with small missing transverse energy are to be expected because the detectors are not perfect: they have a finite resolution. In addition to this there is a resolution from fluctuations inherent in the hadronic shower. Missing transverse energy from these source are expected to be gaussian distributed in x and y . Large missing transverse energy can come from undetected particles e.g. neutrinos or detector imperfections e.g. dead cells.

The missing transverse energy is calculated using the sum of the transverse momentum of the reconstructed particles. For high energy photons and jets, the most accurate determination of the momentum comes from the energy measurement in the calorimeters. The transverse energy of an energy deposit E is calculated as in Equation 3.2. The missing transverse energy is calculated as the negative sum of the transverse energies of all the energy deposits (Equation 3.3).

$$\mathbf{E}_T = E \sin \theta \cos \phi \mathbf{x} + E \sin \theta \sin \phi \mathbf{y} \quad (3.2)$$

$$ME_T = -\sum E_T \quad (3.3)$$

Motivated by SUSY, this search is based on missing energy. In R-parity conserving SUSY models events have decay chains ending in the Lightest Supersymmetric Particle (LSP) which goes undetected and hence shows up as missing transverse energy. In contrast, QCD events (which are the dominant background) have only fake missing energy due to detector imperfections.

3.7 Event Selection

The event selection criteria are listed below.

- Noise Cleaning
- $H_T > 400\text{GeV}$
- ≥ 2 jets
- ≥ 1 photon
- $M_{ET} > 50\text{GeV}$

Three types of noise cleaning are applied to the events.

- **Primary Vertex Selection:** Events are required to have at least one Primary Vertex with $|z| < 24\text{cm}$, $n\text{DOF} > 4$ and $\rho < 2\text{cm}$.
- **HCAL Noise Filter:** There are three types of HCAL noise: HPD noise, RBX noise and PMT window noise. HPD noise comes from the hybrid photodiodes in the HB, HE and HO. Misalignment between the HPD electric field and the external magnetic field can lower the flashover voltage of the HPD resulting in occasional cascades where all or most of the 18 channels within the HPD report large energy deposits. RBX noise is when all or most of the 72 channels in a Readout Box report large energies. The origin of this noise is cross-over in the electronics where a signal causes an induced signal in neighbouring wires. PMT window noise comes from charged particles occasionally hit an HF PMT window directly instead of interacting with the quartz fibres. This results in a large energy deposit in either a long or a short fibre without an appreciable deposit in the other short/long partner. The HCAL noise filter removes HCAL noise by vetoing on variables related to pulse shape, timing, hit multiplicity and number of zero ADC counts.
- **ECAL Spike Cleaning:** ECAL Spikes are isolated energy deposits in the ECAL which do not come from EM showers. The origin of ECAL spikes is pions going directly into the depleted region of the photodetector (without interacting in the ECAL) making it look like there is a significant energy

deposit in the ECAL. ECAL spikes lead to fake photons and fake MET. There are two properties which characterise ECAL spikes: topology and timing. ECAL spikes tend to be single crystal energy deposits in the ECAL which are often not vetoed by the shower shape variable. Some spikes are in time with the rest of the event and some are out of time. The energy varies from a few MeV to a few TeV. A cut of $1 - e4/e1 < 0.96$ is made to avoid ECAL Spikes. $1 - e4/e1$ is the “Swiss Cross” variable in which $e1$ is the highest energy crystal in a 3×3 array and $e4$ is the energy of the four adjacent crystals. Additional spikes with significant energy in two adjacent crystals remained. These residual spikes are vetoed by requiring $e2/e9 < 0.96$ and $|t| < 5\text{ns}$, t is the timing of the signal. This is illustrated by Figure 3.8.

H_T , the scalar sum of the transverse momentum of all the objects in the event, is used as a measure of the energy scale of the event. There is a H_T cut because strongly produced SUSY events have high H_T . The value of this cut is motivated by the desire for the trigger to be fully efficient for the event selection. Figure 3.6 shows that the trigger becomes fully efficient in H_T at around 400GeV.

The ≥ 2 jets cut is well motivated from the SUSY perspective: strongly produced SUSY events start with two squarks/gluinos each of which decay to a quark/gluon (which forms a jet in the detector) and the next SUSY particle in the mass hierarchy. Parameter points with high gluino mass tend to have only 2 jets while those with high squark mass tend to have at least 4 jets.

In strongly produced Gauge Mediated SUSY Breaking the Next-to-Lightest SUSY Particle (NLSP) is the neutralino ($\tilde{\chi}^0$) which decays to a photon and a gravitino. At least two photons are expected in each SUSY event. However, due to the high activity in these events, photons often fall inside the cone of a jet and so only one photon is reconstructed. Hence the ≥ 1 photon cut.

The search is done in bins of MET and H_T , but an initial MET cut is made to avoid the low MET bins where there is no sensitivity due to the huge amount of

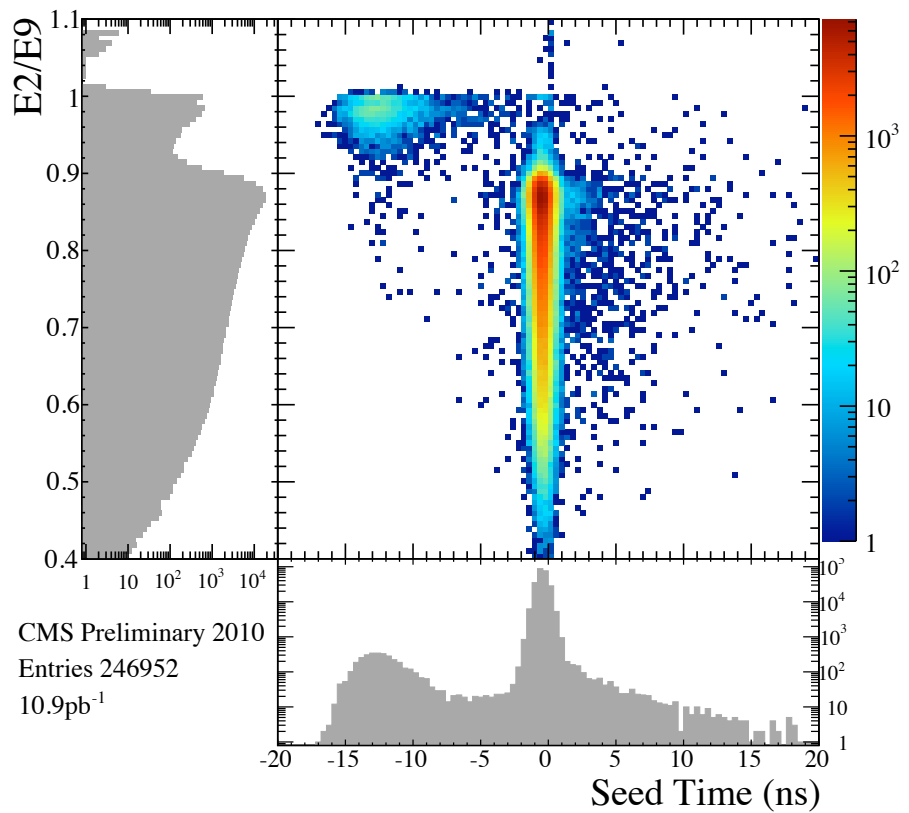


Figure 3.8: A plot of e_2/e_9 vs seed time to show how double crystal ECAL spikes are vetoed.

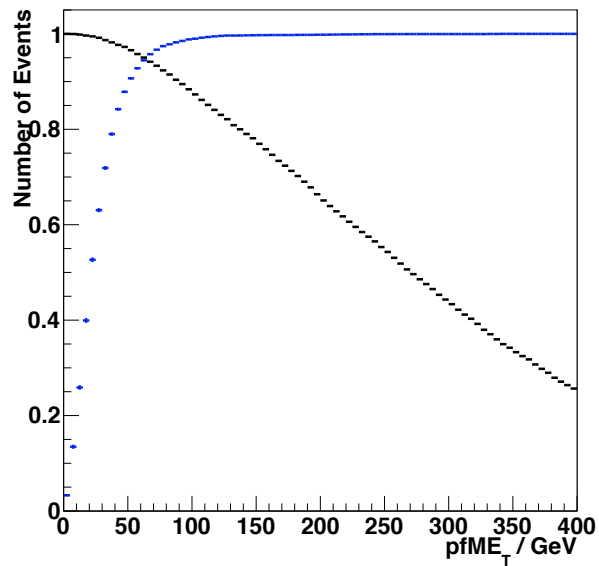


Figure 3.9: The signal efficiency (black) and background rejection (blue) as a function of ME_T cut.

background. Figure 3.9 shows the signal efficiency and the background rejection as a function of ME_T cut.

Chapter 4

Background Estimation

4.1 Introduction

The Standard Model backgrounds to the search are estimated.

QCD is the largest background. QCD events are balanced. Any missing transverse energy comes from detector imperfections. There are three different components to the QCD background:

- **Fakes from jets ($\pi^0 \rightarrow \gamma\gamma$):** π^0 s are one of the main constituents of jets. The two photons from a high energy π^0 can easily be mistaken for a single photon. Most π^0 s in jets will be non-isolated due to the surrounding HCAL energy and tracks. However there is a distribution of isolation and given the large cross section of QCD, some of these events will end up in the isolated tail.
- **Prompt $\gamma+$ jet:** In these events the photon comes directly from the parton hard scattering. The other jet can come from gluon radiation or jet fragmentation. These events contain prompt photons which tend to be isolated and have good shower shape. The p_T of the photons is distributed around half the H_T of the event.
- **QCD jets with ISR/FSR:** A QCD jets event where an initial state quark or final state quark radiates a photon. These events also contain

prompt photons which tend to be isolated and have good shower shape.

The cross section of this process falls with the p_T of the photon.

The Electroweak background is small in comparison to the QCD background. Electroweak processes can contribute real ME_T by the neutrino which is not detected by CMS. The cross section of electroweak processes is much lower than that of QCD and this rules out any background due to fakes from jets. There are two possible sources of photons: $W \rightarrow e\nu$ where the electron has been misidentified as a photon or $W/Z + \gamma$ which is also negligible due to the high H_T requirement.

The $t\bar{t}$ background has real photons and real ME_T , but it is negligible due to the low cross section. The $t\bar{t}$ background is estimated using Monte Carlo.

4.2 QCD Background

All three sources of QCD background have fake ME_T due to detector effects. Fake ME_T can come from the HCAL resolution or from severe mismeasurements such as dead ECAL Trigger Towers or poor HCAL response.

ECAL Trigger Towers are 5×5 arrays of crystals in the ECAL with the photodetectors behind them and the electronics to trigger and read out the data. There are 82×72 trigger towers in the ECAL barrel. Some of these Trigger Towers are dead i.e. there is no data coming from them. This means that any objects going down a dead Trigger Tower will be missed causing fake ME_T . The number of dead Trigger Towers may vary from run to run as those with a problem are masked and those which have been fixed are unmasked. Some ECAL Trigger Towers have long-term problems. There are about XX dead ECAL TTs: YY of these have trigger information available. Figure 4.1 shows a map of ECAL Trigger Towers.

Poor HCAL response is another cause of large fake ME_T . Sometimes a jet is reconstructed with a much lower p_T than it actually has. Such mismeasurements are extremely pathological and not at all well understood. These are not

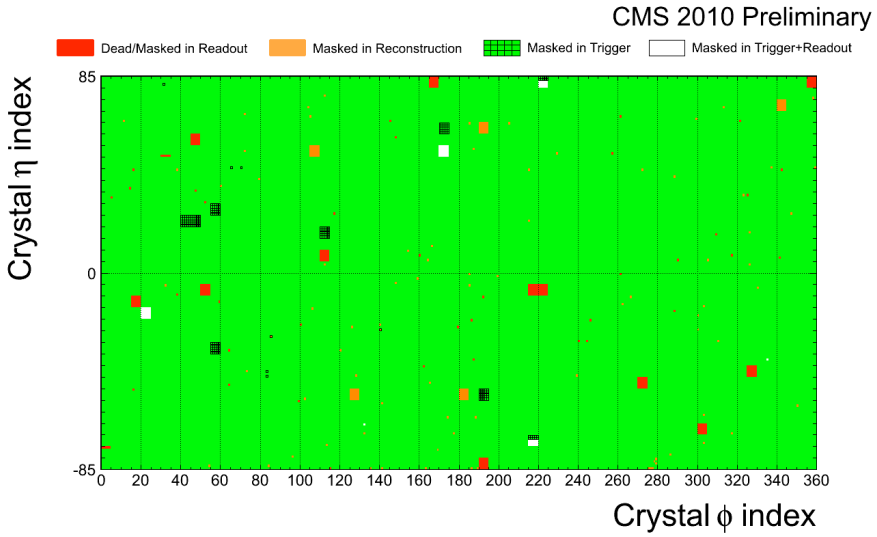


Figure 4.1: A map of the ECAL barrel showing the dead trigger towers. Reproduced from [8].

correlated with any specific region of the detector.

The core resolution is approximately Gaussian in x and y components of MET while the severe mismeasurements contribute a non-Gaussian tail to the MET distribution. Both components scale up with H_T . The core resolution scales as $\sim \sqrt{H_T}$ while the tails increase because higher H_T events contain higher p_T objects which give larger MET when missed.

Any background estimation method needs to be able to estimate these detector effects. If the Monte Carlo were to be used we would be relying on its ability to correctly model all the causes of fake MET . Not just the core resolution but also the MET tail with severe mismeasurements. Using a control sample from data gives a perfect simulation of the CMS detector. The problem is reduced to finding a control sample with the same kinematic properties as the selected sample rather than trying to simulate the most extreme elements of detector response.

A control sample is defined to contain events which pass all the selection criteria except for the isolation. This control sample is used to estimate the ME_T shape of the QCD background in each H_T bin. The absolute number of events is obtained by normalising the ME_T distribution to the number of events with $\text{ME}_T < 50\text{GeV}$.

The assumption in this method is that the control sample has the same ME_T distribution as the selected sample in each H_T bin. The control sample is very similar to the selected sample. It has the same objects with the same kinematic cuts. All events contain at least one photon with good shower shape. The only difference is that in the control sample the photon is non-isolated while in the selected sample it happens to be isolated. Although they contain the three sources of QCD background in different proportions, in both cases the source of ME_T is the same: detector effects. So we can expect them to have the same ME_T distributions.

The background estimation is shown to work in Monte Carlo and in data using a sideband region. Figure 4.2 shows the regions used for the background estimation. The (non-isolated) control sample is used to estimate the background in the (isolated) selected sample. The sideband region is used to check that the background estimation works i.e. the non-isolated and isolated samples have the same ME_T distribution.

Figure 4.3 shows the background estimation and the number of selected events in bins of H_T and ME_T for the Monte Carlo.

Figure 4.4 shows the estimation of the number of isolated events in bins of H_T and ME_T using the non-isolated sample in the sideband region from data compared to the true number of events.

A systematic error on the assumption is taken as half the difference between the estimated number of events and true number of events in Monte Carlo.

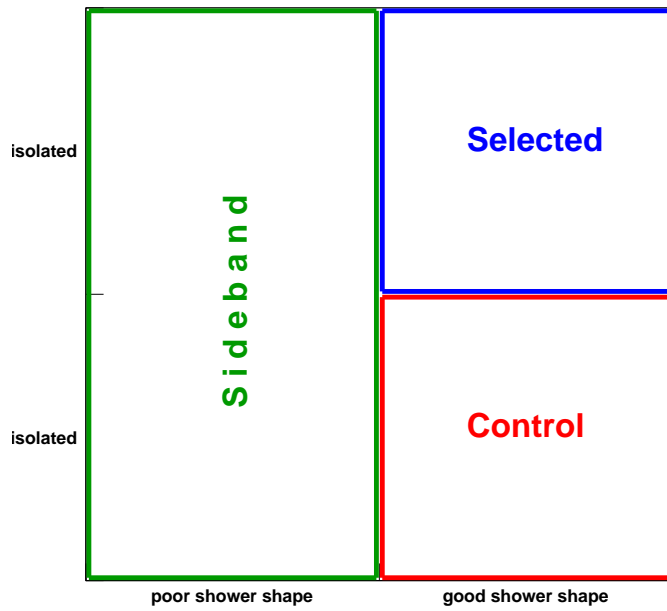


Figure 4.2: A graphic showing the layout of the regions used for the QCD background estimation. The control sample is used to estimate the MET distribution in the selected sample. The sideband region is used to check that the background estimation works.

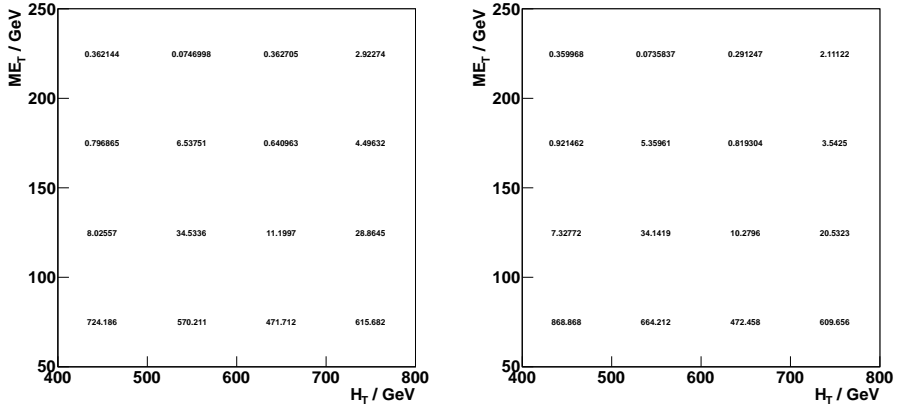


Figure 4.3: The background estimation (left) and number of selected events (right) in bins of H_T and ME_T in the Monte Carlo to check that the background estimation method works.

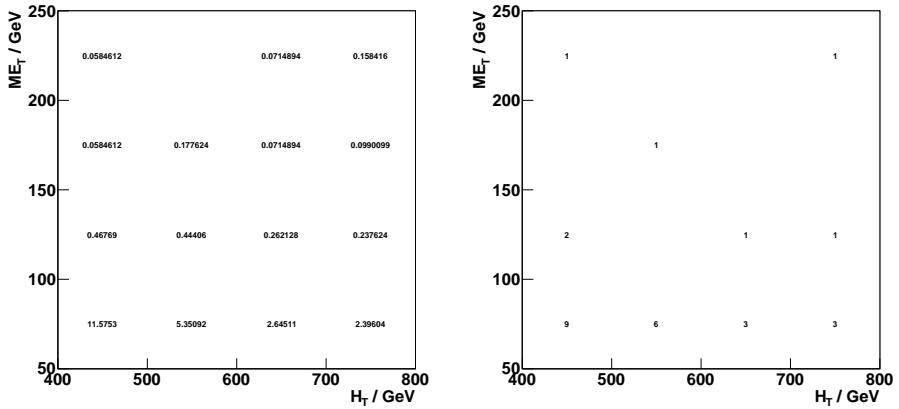


Figure 4.4: The estimation of the number of isolated events (left) using the non-isolated events in the sideband region from data compared to the true number (right).

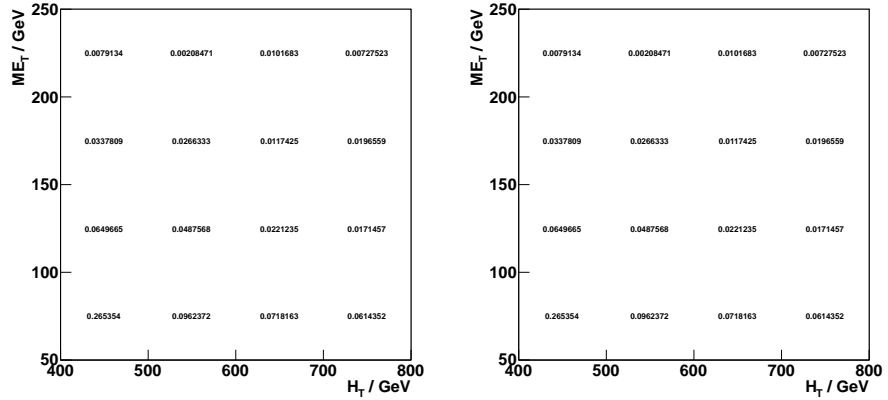


Figure 4.5: The number of events in each (H_T , ME_T) bin for $\gamma W/Z$ (left) and $t\bar{t}$ (right) backgrounds.

4.3 Electroweak and $t\bar{t}$ Backgrounds

Electroweak processes can have real ME_T due to neutrinos which are not detected by CMS. There are two components to the electroweak background: $W \rightarrow e\nu$, where the electron is misidentified as a photon and $\gamma W/Z$, which has a real photon and real ME_T . Then there the $t\bar{t}$ background which also has real ME_T .

The $W \rightarrow e\nu$ background is estimated by measuring the electron/photon misidentification rate in data. The misidentification rate is measured to be 0.014 ± 0.004 [12].

The $\gamma W/Z$ and $t\bar{t}$ backgrounds are estimated from Monte Carlo. The number of events for each of these backgrounds is shown in Figure 4.5.

4.4 Conclusions

Chapter 5

Signal Prediction and Systematics

5.1 Introduction

The predicted number of signal events, s , is given by Equation 5.1.

$$s = \epsilon\sigma L \quad (5.1)$$

where ϵ is the efficiency \times acceptance for the event selection, σ is the cross section and L is the integrated luminosity.

The signal cross section comes from theoretical calculations. 441 different signal models are considered with different values for squark mass and gluino mass. The squark mass and gluino mass each take 21 values from 400 GeV to 2000 GeV in intervals of 80 GeV. The cross section is x-y pb depending on the parameter values. The largest uncertainty in the signal prediction comes from the cross section (10–60%).

The integrated luminosity comes from LHC measurements of the beam. 1.1 fb^{-1} of data is used in this analysis. The uncertainty on the integrated luminosity is about 5%.

The efficiency \times acceptance for the signal is found by applying the selection cuts to the signal MC. Corrections need to be made relating to the difference between the photon efficiency in data and MC and to account for pile-up. In addition to these corrections uncertainties on the signal prediction need to be determined. These include statistical errors and systematic errors. Given that 10,000 events are available for each signal point, the statistical error is small. It is the systematic error on which attention must be focussed.

Cuts are made on jets, photons, H_T and ME_T . The major sources of uncertainty for the jet and H_T cuts are the jet energy scale and jet energy resolution. For the photons the main sources of uncertainty come from the photon efficiency correction for the differences between data and MC and from pile-up which affects the photon isolation efficiency. Both the H_T and ME_T distributions are also affected by pile-up, but this is a small effect.

5.2 Photon Efficiency Correction

The photon efficiency needs to be determined to calculate the signal efficiency. The photon efficiency could be found using the MC, but that relies heavily on the correct modelling of the shower shape, isolation and other variables which may not be well modelled in the MC. The photon efficiency should be measured from data. In the absence of a suitable pure photon sample in the data, electrons from $Z \rightarrow ee$ events are used. This relies on the similarity in detector response between electrons and photons. A scale factor to correct the MC photon efficiency to the real photon efficiency in data is obtained using the electrons (Equation 5.2).

$$\epsilon_{\gamma}^{data} = \frac{\epsilon_e^{data}}{\epsilon_{\gamma}^{MC}} \times \epsilon_{\gamma}^{MC} \quad (5.2)$$

Where:

- ϵ_{γ}^{data} = photon efficiency in data;
- ϵ_{γ}^{MC} = photon efficiency in MC;

- ϵ_e^{data} = electron efficiency obtained using $Z \rightarrow ee$ events in data that satisfy the photon selection;
- ϵ_e^{MC} = electron efficiency obtained using $Z \rightarrow ee$ events in MC that satisfy the photon selection.

The selection critera for electrons are the same as those for photons except that electrons have a track. The distribution in photon or electron identification variables is the similar for isolated photons and electrons. Using $Z \rightarrow ee$ events in data, the tag-and-probe method is used to find the electron efficiency. One electron (tag) is selected with stringent criteria to be sure that it is an electron. Another electron (probe) with looser requirements is located such that the invariant mass of the two electrons lies in the Z peak.

The scale factor is found to be $\epsilon_e^{data}/\epsilon_e^{MC} = 0.953 \pm 0.014(stat.)$ for events with at least one jet. Four possible sources of systematic uncertainty on this number were considered.

Electrons and photons behave differently in MC: Both electrons and photons give EM showers in the ECAL and the selection cuts have been chosen to be similarly efficient for electrons and photons. However, one can imagine that there may be a slight difference between the two e.g. because of bremsstrahlung. To check this effect the MC electron efficiency from $Z \rightarrow ee$ events was compared with the MC photon efficiency from $\gamma + \text{jet}$ events. Half the difference between the two results, 0.5%, was taken as a systematic error on the scale factor.

Pile-up: The MC may not accurately model the data in a high pile-up environment. To estimate the size of this effect the scale factor was calculated for events with fewer than 5 primary vertices and events with at least 5 primary vertices. The number 5 was chosen because that is approximately where the distribution of primary vertices in the data peaks. The difference between the scale factors in the two samples, 0.024, was taken as a systematic error on the scale factor.

Combining the systematic errors above with the statistical error yields a final data-MC efficiency scale factor of $\epsilon_e^{data}/\epsilon_e^{MC} = 0.953 \pm 0.038$.

5.3 Jet Energy Scale

Jets are reconstructed from energy deposits in the calorimeters. p_T and η dependent jet energy corrections are applied to the raw calorimeter energy to get the jet energy. Any variation in these corrections would change the jet p_T , the H_T and the ME_T .

The appropriate jet energy corrections are determined from γ +jet events in data. The photon is well measured and the event is balanced (within the ME_T resolution). Details of the procedure to determine the jet energy corrections and their uncertainties are given in [7]. This corresponds to $\sim 3\%$ uncertainty on jets above 50GeV and $\sim 5\%$ uncertainty on smaller jets and unclustered energy. Figure 5.1 shows the jet energy correction factors as a function of jet p_T for jets with ($|\eta| = 1.0$) and as a function of η for jets with $p_T = 200$ GeV (the core of the jet distribution).

Figure 5.2 shows the total jet energy scale uncertainty against jet p_T for central jets.

The jet energy scale uncertainties have no impact on the background estimation because that is determined through a data-driven method. However the effect on the number of expected signal events needs to be evaluated.

The p_T of all the jets is modified upward and downward according to the jet energy uncertainties before applying the event selection. The ME_T can be expressed as Equation 5.3.

$$ME_T = -\sum \text{jets} - \text{photon} - \text{unclustered energy} \quad (5.3)$$

The ME_T is modified to take account of the jet energy correction uncertainties by the following procedure.

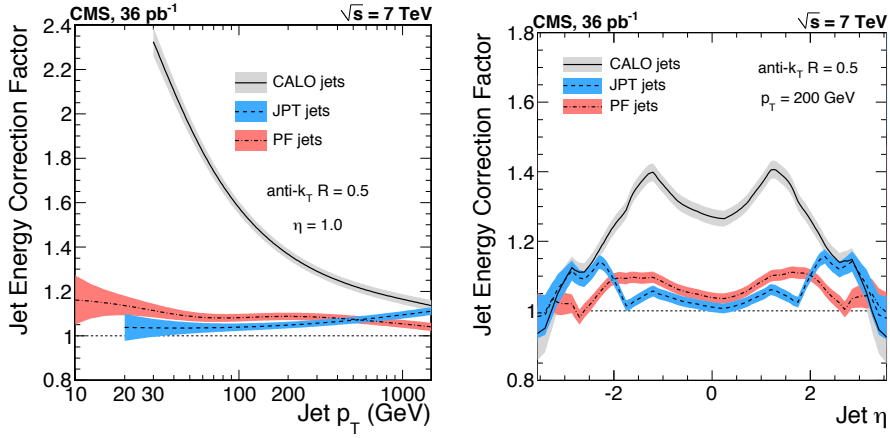


Figure 5.1: The jet energy correction factor as a function of p_T with $\eta = 1.0$ (left) and as a function of η with $p_T = 200\text{GeV}$ (right). Three different jet reconstructions are shown: CALO, JPT and PF. PF jets are used in this analysis. The bands indicate the corresponding uncertainties.

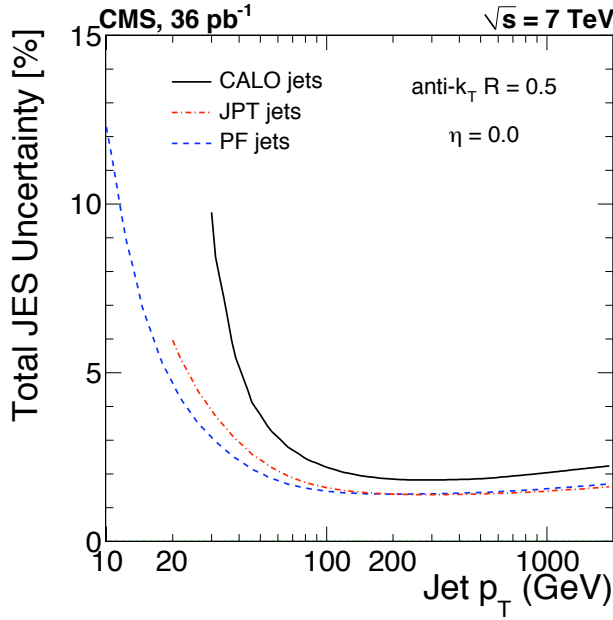


Figure 5.2: The total jet energy scale uncertainty as a function of p_T for central jets. Three different jet reconstructions are shown: CALO, JPT and PF. PF jets are used in this analysis.

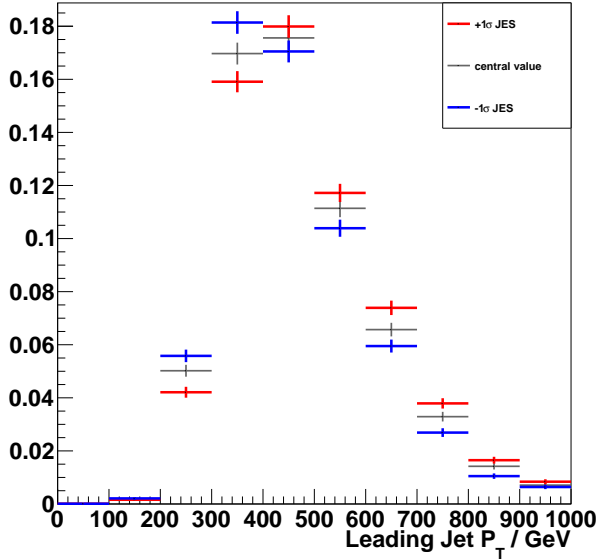


Figure 5.3: The leading jet p_T distribution in signal events with a one sigma upward variation (red) and one sigma downward variation (blue) in jet energy scale.

- Add the photon to the ME_T (i.e. remove it from consideration).
- Add the jets also to get the unclustered energy.
- Modify the unclustered energy by 5%.
- Subtract the jets scaled according to the jet energy correction uncertainties.
- Subtract the photon to get the modified ME_T .

Figure 5.3 shows the leading jet p_T distribution with a one sigma upward variation and a one sigma downward variation in jet energy scale. Figure 5.4 shows how the variation in jet energy scale affects the ME_T and H_T distributions.

The important result is how the variation in jet energy scale affects the signal efficiency in each (H_T, ME_T) bin. Figure 5.5 shows these numbers. The jet energy scale uncertainties are correlated across all (H_T, ME_T) bins.

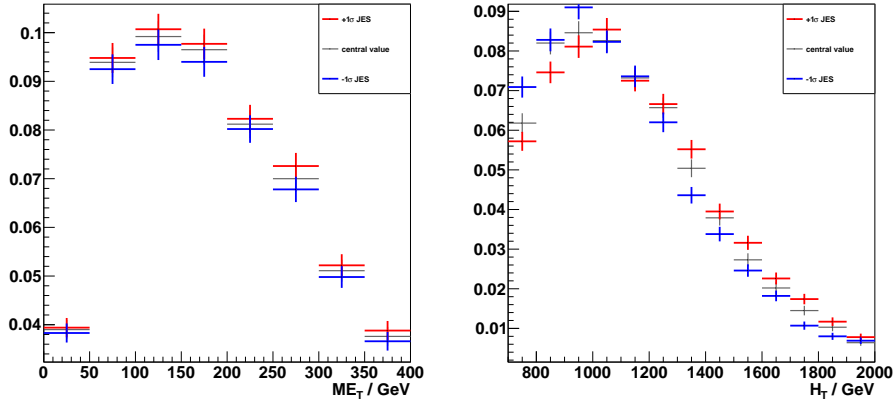


Figure 5.4: The ME_T distribution (left) and H_T distribution (right) in signal events with a one sigma upward variation (red) and one sigma downward variation (blue) in jet energy scale.

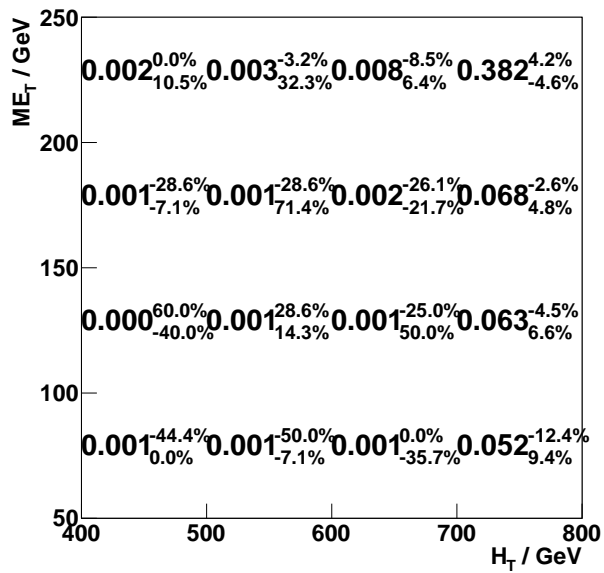


Figure 5.5: The percentage change in the signal efficiency when the jet energy scale is varied by $\pm 1\sigma$, where σ is the jet energy scale uncertainty.

5.4 Jet Energy Resolution

The jet p_T resolution is determined using two different methods:

- **Di-jet asymmetry:** This method uses balanced di-jet events which are abundant in data and considers p_T conservation. An asymmetry variable is constructed from the p_T of the two jets:

$$A = \frac{p_T^1 - p_T^2}{p_T^1 + p_T^2} \quad (5.4)$$

The variance of the asymmetry variable can be expressed as:

$$\sigma_A^2 = \left(\frac{\partial A}{\partial p_T^1} \right)^2 \sigma_{p_T^1}^2 + \left(\frac{\partial A}{\partial p_T^2} \right)^2 \sigma_{p_T^2}^2 \quad (5.5)$$

For jets which lie in the same η bin and the same p_T bin, the p_T 's are the same and the resolutions are the same so there is an expression for the fractional p_T resolution in terms of the variance in the asymmetry.

$$\frac{\sigma p_T}{p_T} = \sqrt{2}\sigma_A \quad (5.6)$$

The asymmetry and the variance in the asymmetry are quantities that can be measured in data.

- **γ/Z +jet balance:** This method uses γ +jet or Z +jet events from data and uses the γ or Z as a well measured reference object to which the jet p_T can be compared. In balanced events the γ/Z has the same p_T as the jet. The ratio, R , of the jet p_T relative to the γ/Z p_T in bins of γ/Z p_T gives the jet p_T resolution.

$$R = \frac{p_T^{jet}}{p_T^{\gamma/Z}} \quad (5.7)$$

Further details on the jet p_T resolution measurement and determination of the associated uncertainty can be found in [7]. The jet p_T resolution as a function of jet p_T and for $|\eta| < 0.5$ is shown in Figure 5.6. The figure also shows that MC agrees well with the data as far as jet energy resolution is concerned. For the SUSY events the “true” jet energy comes from the generator level in the MC. The jet energy resolution is determined by comparing the reconstructed

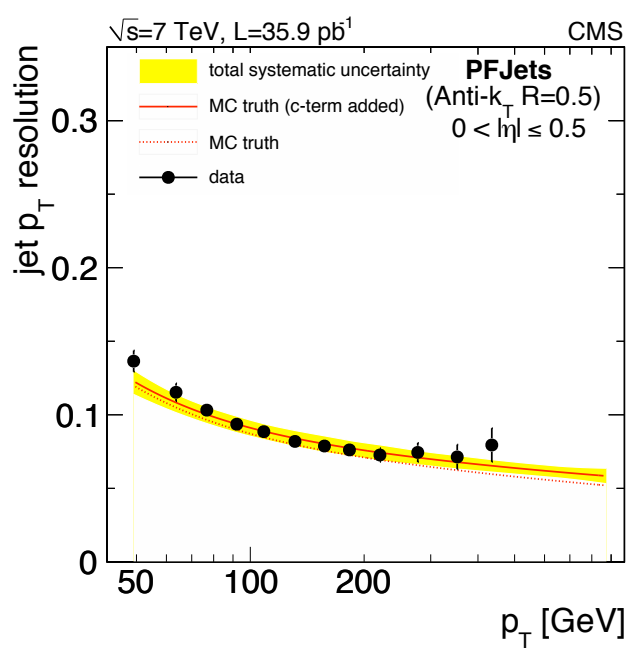


Figure 5.6: The jet energy resolution measured from data for jets with $|\eta| < 0.5$ (black points) compared to MC (red line). The yellow band gives the systematic uncertainty. Reproduced from [7].

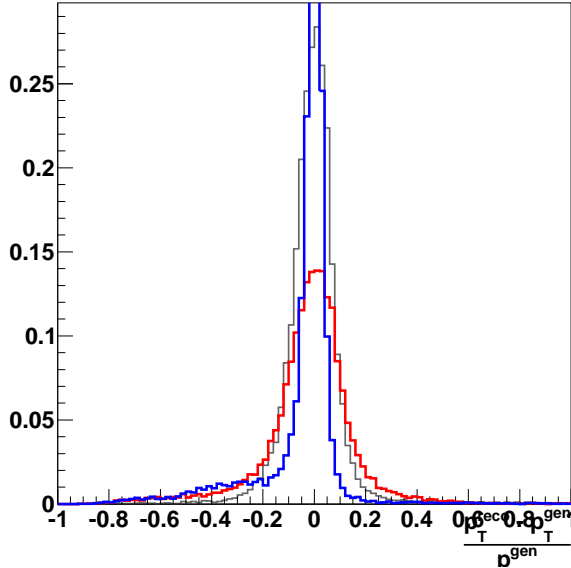


Figure 5.7: The jet p_T resolution compared to generator level jets (grey) and the same distribution after an upward (red) and downward (blue) variation of 50% in the jet p_T resolution.

jet energy with the generator level jet energy. This gives a jet p_T resolution similar to that measured in [7].

The resolution is varied upward and downward by 50%, which correspond to the uncertainty on the forward jets but is conservative for the central jets. The variation in resolution is made by changing $\frac{p_T^{reco} - p_T^{gen}}{p_T^{gen}}$ by 50% for each jet. Figure 5.7 shows the jet energy resolution with an upward and a downward variation.

Figure 5.8 shows the effect of the variation in resolution on the H_T and ME_T distributions. The important result is how the variation in jet energy scale affects the signal efficiency in each (H_T , ME_T) bin. Figure 5.5 shows these numbers. The jet energy scale uncertainties are correlated across all (H_T, ME_T) bins.

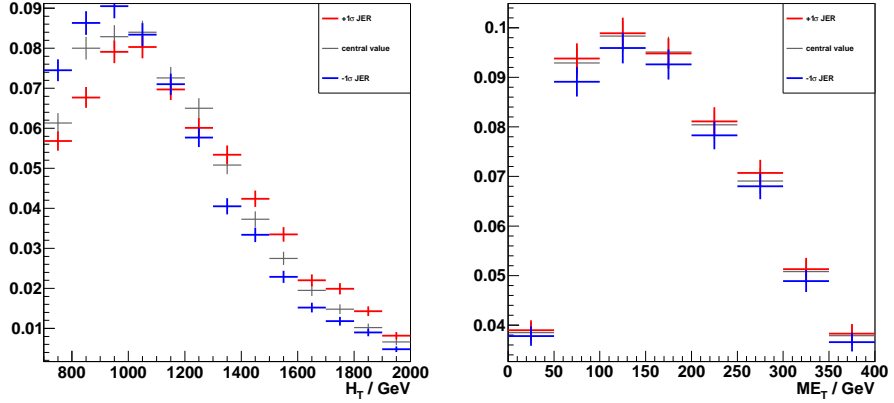


Figure 5.8: The effect of an upward (red) and a downward (blue) variation of the jet p_T resolution on the H_T and MET distributions.

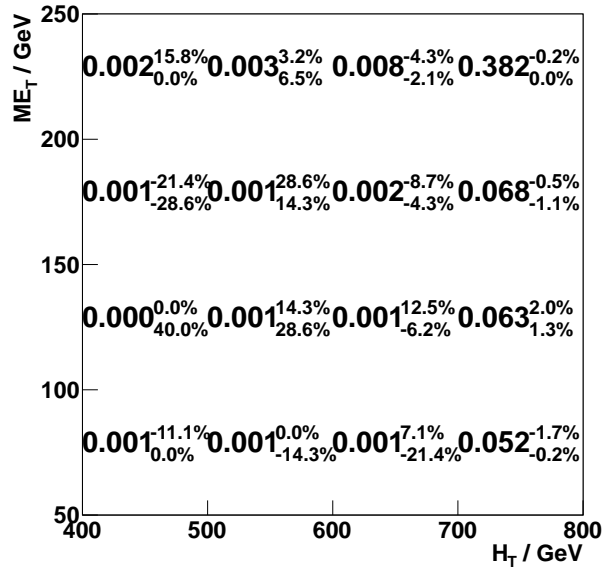


Figure 5.9: The percentage change in the signal efficiency when the jet p_T resolution is varied by $\pm 1\sigma$, where σ is the jet p_T resolution uncertainty.

5.5 Pile-up

Pile-up is where there are multiple interactions per bunch crossing. Pile-up affects the number of signal events in several ways:

- The H_T increases due to jets and underlying event activity from other interactions in the same bunch crossing.
- The MET distribution is broadened by the introduction of more jets and underlying event activity.
- The photon isolation efficiency is reduced since there is more surrounding activity which can populate the isolation cone.

Most of the pile-up events will be soft QCD with low p_T jets approximately parallel to the beam-line. These do not have a huge effect on the H_T since the H_T is a sum of high p_T jets. The effect of pile-up on the H_T is evaluated by looking at the H_T distribution in MC QCD events with and without pile-up. A shift of 7.0 ± 0.8 is applied to the no pile-up H_T distribution to match the pile-up H_T distribution (Figure 5.10). Figure 5.11 shows the H_T distribution with a ± 1 sigma variation in the shift.

The MET distribution is broadened by the introduction of more jets from other interactions in the same bunch crossing. The pile-up events will mostly be low H_T and balanced so will have only a little effect on the MET . The MET distribution is smeared to account for pile-up. To determine the amount of smearing necessary a QCD sample with similar H_T and no pile-up is smeared until the shape agrees with the MET distribution with pile-up. Figure 5.13 shows the average MET in QCD events without pile-up as a function of the MET smearing. From the plot a MET smearing of $2.9 \pm 0.8\%$ is applied to account for pile-up. Figure 5.14 shows the MET distribution with a ± 1 sigma variation in the shift.

The photon isolation efficiency is particularly affected by pile-up because activity from other events in the same bunch crossing can populate the isolation cone. To quantify this effect QCD MC events with a similar H_T were used to determine the photon efficiency in MC as a function of the number of pri-

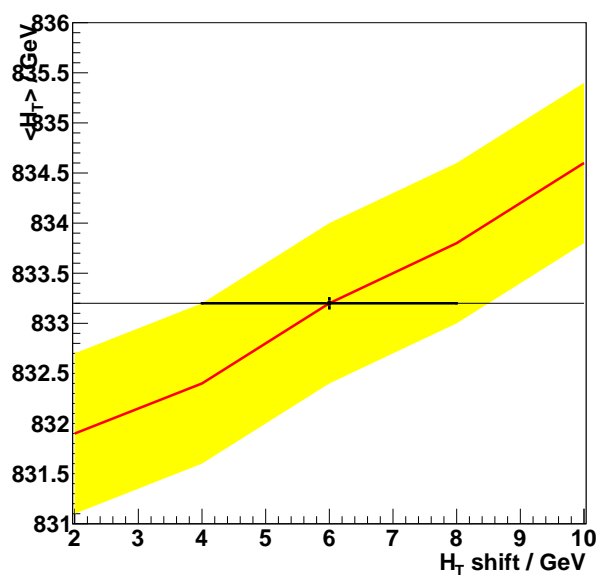


Figure 5.10: The mean H_T as a function of H_T shift (red) with one sigma band (yellow) in QCD events with a similar H_T to the signal. The mean H_T with pile-up is shown in black.

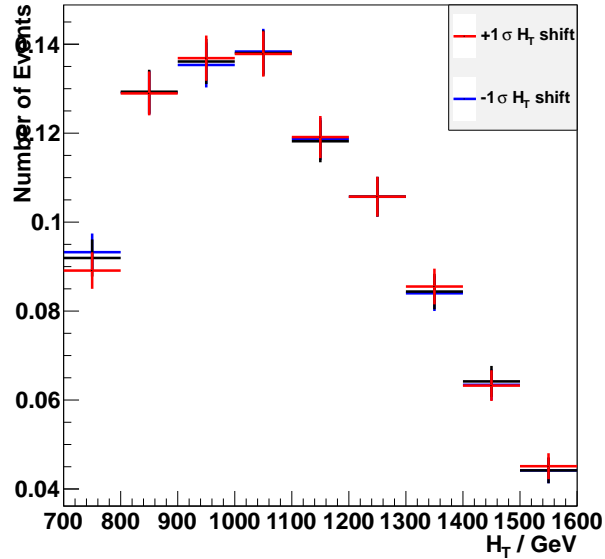


Figure 5.11: The correction to the H_T distribution to account for pile-up. The ± 1 sigma variations are shown in red and blue respectively.

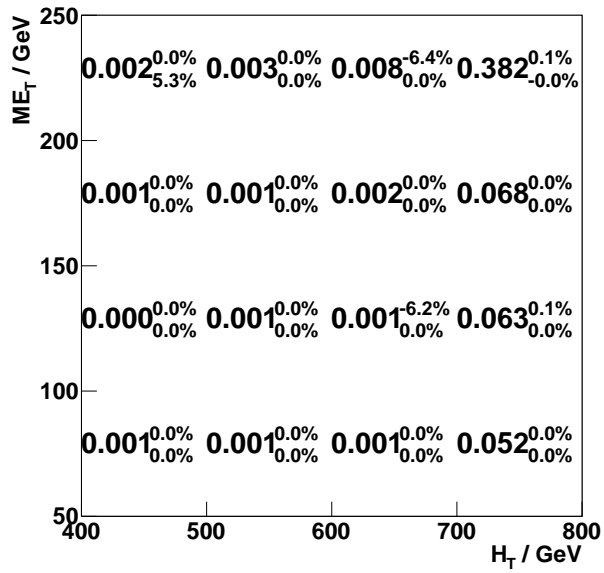


Figure 5.12: The percentage change in the signal efficiency when the H_T shift to account for pile-up is varied within its uncertainty.

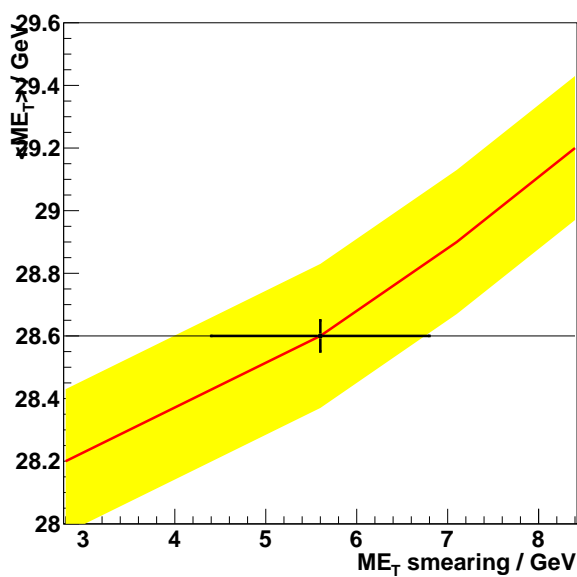


Figure 5.13: The mean ME_T as a function of ME_T smearing (red) with one sigma band (yellow) in QCD events with a similar H_T to the signal. The mean ME_T with pile-up is shown in black.

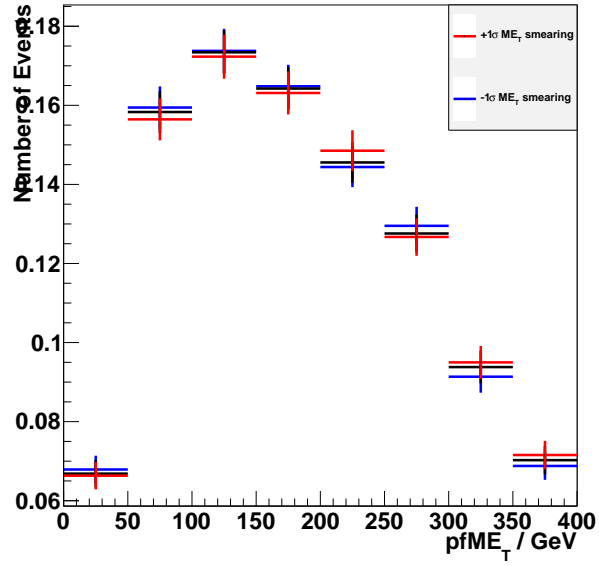


Figure 5.14: The correction to the ME_T distribution to account for pile-up. The ± 1 sigma variations are shown in red and blue respectively.

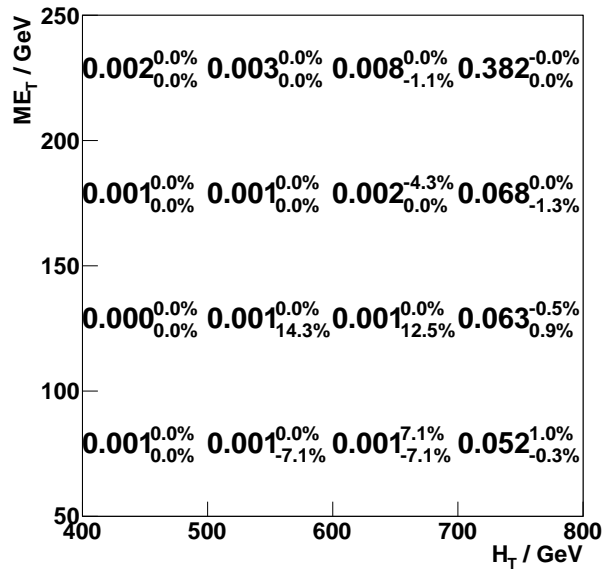


Figure 5.15: The percentage change in the signal efficiency when the ME_T smearing to account for pile-up is varied within its uncertainty.

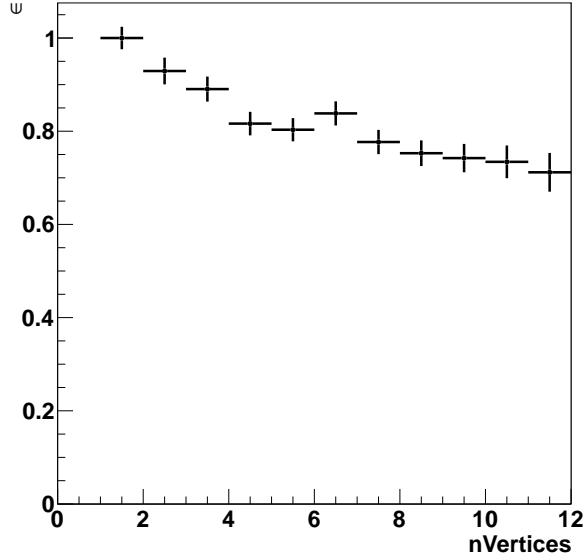


Figure 5.16: The relative photon efficiency as a function of the number of primary vertices.

mary vertices. Figure 5.16 shows the relative efficiency as a function of the number of primary vertices. Taking the distribution of number of primary vertices from data, the efficiency expected under pile-up can be calculated. This method assumes that SUSY photons have a similar behaviour under pile-up to QCD photons. This assumption is reasonable because the pile-up affects mainly the isolation through extra surrounding activity which is a property of the event rather than the photon. This method also relies on MC modelling the photon efficiency in pile-up well. This can be checked by looking at Zee events in data. The efficiency requires only a small correction between data and MC which is relatively stable with respect to pile-up (Figure 5.17). The efficiency correction due to pile-up is found to be $0.83 \pm 0.01(\text{stat.}) \pm 0.01(\text{syst.})$.

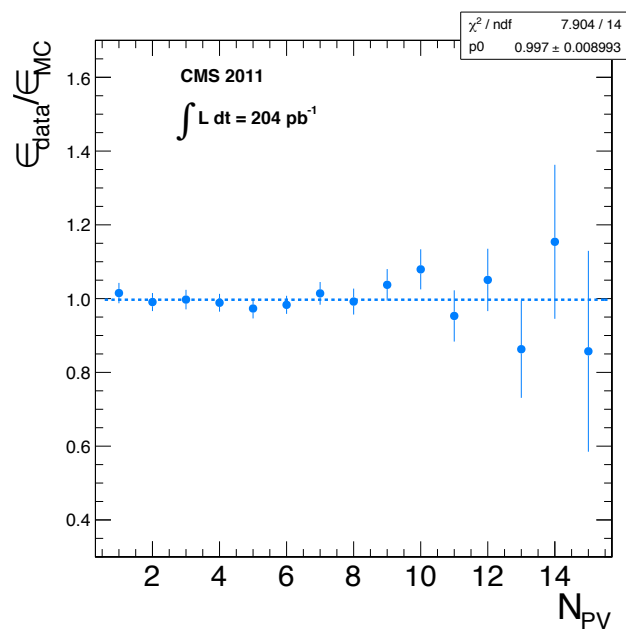


Figure 5.17: The efficiency correction between data and MC as a function of the number of primary vertices.

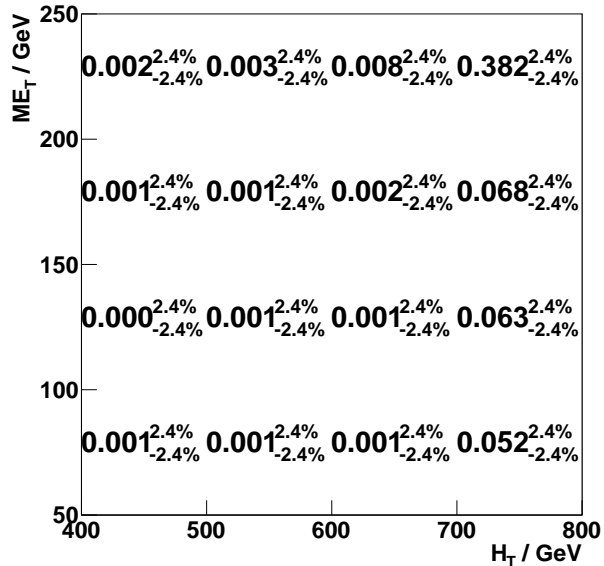


Figure 5.18: The percentage change in the signal efficiency when the photon efficiency under pile-up is varied within its uncertainty.

5.6 Signal Cross-Section

Write how the cross-section is calculated.

There is a theoretical uncertainty on the signal cross-section due to the uncertainty on the PDF distributions. Figure 5.19 shows the percentage uncertainty on the cross-section for each parameter point in the mSquark vs mGluino plane.

5.7 Integrated Luminosity

There are a number of different ways of measuring the LHC luminosity. The method used for early data was to use LHC beam parameters. The luminosity is given by:

$$L = \frac{N^2 n_b f}{A_{eff}} \quad (5.8)$$

where N is the number of particles in each of the colliding bunches, n_b is the

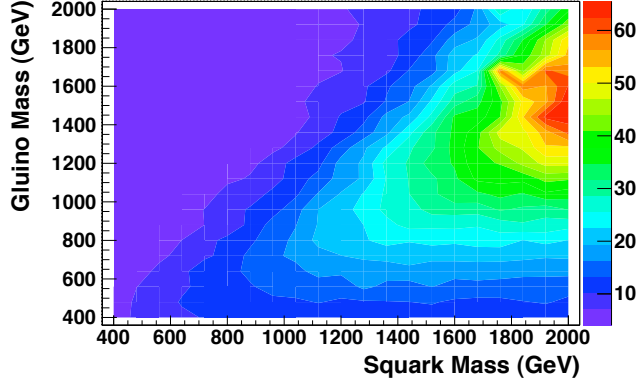


Figure 5.19: The percentage uncertainty on the signal cross-section based on PDF uncertainties for each parameter point in the mSquark vs mGluino plane. Reproduced from [12].

number of bunches, f is the revolution frequency of the beams and A_{eff} is the effective transverse area in which the collisions occur.

The revolution frequency and the number of bunches are known precisely (to $\sim 1\%$) from measurements of the beam current. The limiting uncertainty for the luminosity measurement is that of A_{eff} . The beam sizes must be controlled to 20-30% for safe operation of the LHC. A_{eff} is measured using van der Meer scans of the transverse beam profile [16]. Assuming a gaussian transverse beam profile, A_{eff} can be calculated as $A_{eff} = 4\pi\sigma_x\sigma_y$. The uncertainty on the integrated luminosity measurement for this method is 10%.

The measurement can be improved using TOTEM and W/Z leptonic decays as standard candles. TOTEM is a forward detector 240m from the interaction point designed to measure the total proton-proton cross-section. By monitoring the cross-section over time the integrated luminosity can be estimated. There are still acceptance and PDF uncertainties associated with the cross-section measurement but these give a much smaller error on the integrated luminosity. The uncertainty from this method is 4%.

| Source of Systematic Uncertainty | QCD | EWK | SUSY |
|------------------------------------|-----|------|------|
| QCD Background Estimation | 5% | - | - |
| e/ γ Misidentification | - | 30% | - |
| $W \rightarrow e\nu$ Cross-Section | - | | - |
| Photon Efficiency | - | 3.8% | 3.8% |
| Jet Energy Scale | - | | 4.4% |
| Jet Energy Resolution | - | | 0.1% |
| Pile-up: HT shift | - | | 0.1% |
| Pile-up: MET smearing | - | | 0.0% |
| Pile-up: photon efficiency | - | | 2.4% |
| Signal Cross-Section | - | - | 20% |
| Integrated Luminosity | - | 5% | 5% |

Table 5.1: A summary of the systematic uncertainties and how they affect the expected number of events in the signal and each of the backgrounds.

5.8 Summary of Systematics

Table 5.1 shows a summary of all the systematic uncertainties for the backgrounds and the signal. For simplicity the systematic uncertainties for only the most significant bin in terms of the limit setting (H_T , ME_T) = (700+, 200+) are shown.

Chapter 6

Limit Setting and Results

6.1 Introduction

Once the event selection and background estimation procedure have been defined and the data has been collected one needs to determine the limit on the cross section of a possible SUSY signal (according to a specific model) or, if a discovery has been made, the significance of that discovery.

In the present case no discovery has been made so a limit on the cross section must be found. There are various statistical procedures for doing this and no consensus on the best method. If all methods give similar results, then it does not matter which method is used.

A likelihood function must be defined. The likelihood is the probability of observing the data given a model. This encompasses the statistical uncertainties and the background model as well as the systematic uncertainties associated with the detector (e.g. luminosity measurement and jet energy scale uncertainty) which affect the number of signal events expected.

Parameters in the likelihood should include the parameter of interest on which we wish to set a limit – the cross section in this case – in addition to other unknowns associated with systematic uncertainties.

The goal is to find a confidence interval for the parameter of interest based on the likelihood. This tells us an upper limit on the cross section of a possible SUSY signal at a given confidence level.

Three methods are used here for limit setting:

- Profile Likelihood using Wilks Theorem to find the confidence interval.
- Feldman Cousins Method: using Neyman Construction to get the confidence interval with the Profile Likelihood as a test statistic.
- CLs with MC toys using the Profile Likelihood.

6.2 Likelihood Function

We are looking for a signal in N bins, labelled $i = 1..N$.

Let:

- b_i = Estimated number of background events in bin i;
- s_i = Number of expected signal events in bin i according to a specific SUSY model;
- n_i = Number of events observed in bin i;

Considering only the statistical error on the number of observed events given an expected number of events, which follows a Poisson distribution, the likelihood for the background only hypothesis is given by Equation 6.1.

$$L_b = \prod_{i=1}^N p(n_i|b_i) = \prod_{i=1}^N \frac{b_i^{n_i} e^{-b_i}}{n_i!} \quad (6.1)$$

And for the signal plus background hypothesis the likelihood is given by Equation 6.2.

$$L_{s+b} = \prod_{i=1}^N p(n_i|s_i + b_i) = \prod_{i=1}^N \frac{(s_i + b_i)^{n_i} e^{-(s_i + b_i)}}{n_i!} \quad (6.2)$$

The number of signal events is obtained by applying the selection to the signal Monte Carlo. It depends on the signal efficiency times acceptance ϵ_i , the cross section σ and the integrated luminosity $\int L dt$ as in Equation 6.3.

$$s_i = \epsilon_i \cdot \left(\int L dt \right) \cdot \sigma \quad (6.3)$$

The likelihood for the signal plus background hypothesis can now be written as Equation 6.4.

$$L_{s+b} = \prod_{i=1}^N \frac{(\epsilon_i \cdot (\int L dt) \cdot \sigma + b_i)^{n_i} e^{-(\epsilon_i \cdot (\int L dt) \cdot \sigma + b_i)}}{n_i!} \quad (6.4)$$

6.3 Systematic Uncertainties

Consider M sources of systematic uncertainty: σ_j , $j = 1..M$. Systematic uncertainties can be introduced to the likelihood as nuisance parameters θ_j upon which b_i and s_i depend. Gaussian terms are added to the likelihood to constrain their values. For example if the integrated luminosity was measured to be 1.1fb^{-1} with an error of 4%, a Gaussian term with mean 1100 and sigma 44 would be added to the likelihood. Thus the central value of the luminosity is allowed to fluctuate constrained by the Gaussian. Equation 6.5 shows the full likelihood function, including nuisance parameters.

$$L_{s+b} = \prod_{i=1}^N \frac{(\epsilon_i \cdot (\int L dt) \cdot \sigma + b_i)^{n_i} e^{-(\epsilon_i \cdot (\int L dt) \cdot \sigma + b_i)}}{n_i!} \cdot \prod_{j=1}^M \frac{1}{\sqrt{2\pi}\sigma_j} e^{-\frac{1}{2}\left(\frac{\theta_j - \mu_j}{\sigma_j}\right)^2} \quad (6.5)$$

6.4 Test Statistic

A confidence interval is calculated based on a test statistic. This can be the likelihood for the signal + background hypothesis. However this can be misleading if the background hypothesis doesn't fit either. A more common approach is to use the likelihood ratio (Equation 6.6), where $\boldsymbol{\theta}$ is the vector of parameters and $\hat{\boldsymbol{\theta}}$ is the vector of parameter values which maximises the likelihood.

$$-2 \log \Lambda_{profile} = -2 \log \frac{L_{s+b}(\theta)}{L_b(\hat{\theta})} \quad (6.6)$$

For ease of calculation the negative log likelihood is used instead of the likelihood. Both the likelihood and the negative log likelihood must have an optimum at the same value whatever the form of the likelihood function since the logarithm is a monotonic function.

6.5 Confidence Intervals

6.5.1 Wilks Theorem

Wilks Theorem states that the negative log profile likelihood ratio is asymptotically distributed as a χ^2 with N degrees of freedom, where N is the number of parameters of interest.

6.5.2 Neyman Construction

Consider a pdf $f(x; \theta)$ where θ is the unknown parameter we are trying to estimate: the cross section in our case. We wish to construct a confidence interval for θ .

Step through possible values of θ . For each value of θ find a range (x_1, x_2) such that a fraction $1 - \alpha$ of the x distribution lies within the range, see Equation 6.7. $1 - \alpha$ is the confidence level.

$$\int_{x_1}^{x_2} f(x; \theta) dx = 1 - \alpha \quad (6.7)$$

Figure 6.1 shows the ranges (x_1, x_2) as horizontal line segments on the (x, θ) plane for each possible value of θ .

Upon measurement of x as having value x_0 we draw a vertical line on the (x, θ) plane (Figure 6.1) at $x = x_0$. Under the Neyman Construction the confidence interval for θ is defined by the values of θ where the vertical line intersects the horizontal ranges (x_1, x_2) .

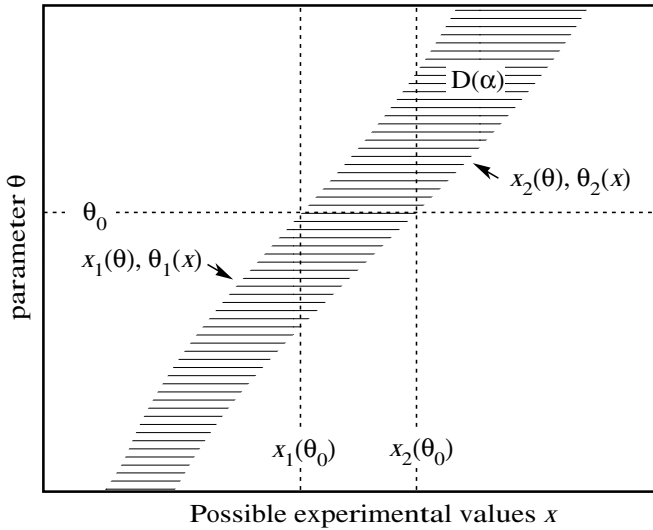


Figure 6.1: The ranges (x_1, x_2) as horizontal lines in the (x, θ) plane for each possible value of θ . A confidence belt is marked out the vertical height of which gives the confidence interval for each possible measurement value.

The Neyman Construction is not a unique procedure: it does not specify how the ranges (x_1, x_2) which contain $1 - \alpha$ of the pdf should be found. A rule for ordering the x values (test statistic) is required.

In the Feldman Cousins method the ordering principle is the likelihood ratio – motivated by the Neyman-Pearson lemma. When nuisance parameters are involved the profile likelihood ratio is the natural generalisation.

6.5.3 CLs: MC toys with hypothesis testing

6.6 Expected and Observed Limit

An expected limit without looking at the data can be calculated. Pseudo data is generated using the background model. An expected limit is calculated using any of the above methods using the pseudo data as if it were data.

Many sets of pseudo data are generated and a limit on the cross section of a

possible SUSY signal is calculated for each. An expected limit can be drawn on the SUSY parameter space by linking those parameter points for which the cross section can be excluded at 95% confidence level in half of the pseudo experiments – the median of excluded cross section across all pseudo experiments. 1σ and 2σ bands, lines linking the parameter points where the cross section is excluded for 67% and 95% of the pseudo experiments respectively, are also drawn.

Chapter 7

Conclusions and Further Work

Write conclusions here.

Bibliography

- [1] The worldwide lhc computing grid. URL: <http://lcg.web.cern.ch/lcg/>.
- [2] 1998.
- [3] 2002.
- [4] The CMS Collaboration. *CMS Physics Technical Design Report Volume 1: Detector Performance and Software*. CERN, 2006.
- [5] The CMS Collaboration. The cms experiment at the cern large hadron collider. *JISNT* 3, 2008. S08003.
- [6] The CMS Collaboration. Precise mapping of the magnetic field in the cms barrel yoke using cosmic rays. 2009. CMS PAPER CFT-09-015.
- [7] The CMS Collaboration. Determination of jet energy calibration and transverse momentum resolution in cms. 2010. CMS PAS JME-10-011.
- [8] The CMS Collaboration. Electromagnetic calorimeter commissioning and first results with 7tev data. 2010. CMS NOTE 2010/012.
- [9] The CMS Collaboration. Met resolution vs. sumet in minimum bias 7 tev events. 2010. CMS PAS JME-10-003.
- [10] The CMS Collaboration. Met resolution vs. sumet in minimum bias 7 tev events. 2010. CMS AN AN-10-142.
- [11] The CMS Collaboration. A review of clustering algorithms and energy corrections in the electromagnetic calorimeter. 2010. CMS IN 2010/008.

- [12] The CMS Collaboration. Search for general gauge mediated supersymmetry with two photons and missing transverse energy. 2010. CMS NOTE AN-11-289.
- [13] The CMS Collaboration. Tracking and vertexing results from first collisions. 2010. CMS PAS TRK-10-001.
- [14] V. I. Klyukhin et. al. Measurement of the cms magnetic field. *IEEE Trans. on applied Superc. 18*, page 395, 2008. No 2.
- [15] Leslie Lamport. \LaTeX : A document preparation system. 1986.
- [16] S. Van Der Meer. icalibration of the eective beam height in the isr. *ISR-PO/68-31*, 1968.
- [17] E. Noether. Invariante variationsprobleme. *Nachr. v. d. Ges. d. Wiss. zu Gttingen*, 1918.
- [18] Oren Patashnik. Designing bibtex styles. January 1988. The part of BibTeX's documentation that's not meant for general users.
- [19] Oren Patashnik. Using BibTeX. January 1988. Documentation for general BibTeX users.
- [20] S.Mrenna T. Sjostrand and P. Skands. Pythia 6.4 physics and manual. *JHEP05*, 2006.